Commun. Comput. Phys.
doi: 10.4208/cicp.OA-2017-0102

Vol. **22**, No. 5, pp. 1175-1223
November 2017

A Unified Gas Kinetic Scheme for Continuum and Rarefied Flows V: Multiscale and Multi-Component Plasma Transport

Chang Liu[1] and Kun Xu[1,2,*]

[1] *Department of Mathematics, Hong Kong University of Science and Technology, Clear Water Bay, Kowloon, Hong Kong.*
[2] *Department of Mechanical and Aerospace Engineering, Hong Kong University of Science and Technology, Clear Water Bay, Kowloon, Hong Kong.*

Received 5 May 2017; Accepted (in revised version) 17 July 2017

Abstract. As a continuation of developing multiscale method for the transport phenomena, a unified gas kinetic scheme (UGKS) for multi-scale and multi-component plasma simulation is constructed. The current scheme is a direct modeling method, where the time evolution solutions from the Vlasov-BGK equations of electron and ion and the Maxwell equations are used to construct a scale-dependent plasma simulation model. The modeling scale used in the UGKS is the mesh size scale, which can be comparable to or much larger than the local mean free path. As a result, with the variation of modeling scales in space and time through the so-called cell's Knudsen number and normalized Larmor radius, the discretized governing equations can recover a wide range of plasma evolution from the Vlasov equation in the kinetic scale to different-type of magnetohydrodynamic (MHD) equations in the hydrodynamic scale. The UGKS provides a general evolution model, which goes to the Vlasov equation in the kinetic scale and many types of MHD equations in the hydrodynamic scale, such as the two fluids model, the Hall, the resistive, and the ideal MHD equations. All current existing governing equations become the subsets of the UGKS, and the UGKS bridges these distinguishable governing equations seamlessly. The construction of UGKS is based on the implementation of physical conservation laws and the un-splitting treatment of particle collision, acceleration, and transport in the construction of a scale-dependent numerical flux across a cell interface. At the same time, the discretized plasma evolution equations are coupled with the Maxwell equations for electro-magnetic fields, which also cover a scale-dependent transition between the Ampère's law and the Ohm's law for the calculation of electric field. The time step of UGKS is not limited by the relaxation time, the cyclotron period, and the speed of light in the ideal-MHD regime. Our scheme is able to give a physically accurate solution for plasma simulation with a wide range of Knudsen number and normalized Larmor radius. It can be used to study the phenomena from the Vlasov limit to the

*Corresponding author. *Email addresses:* cliuaa@connect.ust.hk (C. Liu), makxu@ust.hk (K. Xu)

 ©2017 Global-Science Press

https://doi.org/10.4208/cicp.OA-2017-0102 Published online by Cambridge University Press

scale of plasma skin depth for the capturing of two-fluid effect, and the phenomena in the plasma transition regime with a modest Knudsen number and Larmor radius. The UGKS is validated by numerical test cases, such as the Landau damping and two stream instability in the kinetic regime, and the Brio-Wu shock tube problem, and the Orszag-Tang MHD turbulence problem in the hydrodynamic regime. The scheme is also used to study the geospace environment modeling (GEM), such as the challenging magnetic reconnection problem in the transition regime. At the same time, the magnetic reconnection mechanism of the Sweet-Parker model and the Hall effect model can be connected smoothly through the variation of Larmor radius in the UGKS simulations. Overall, the UGKS is a physically reliable multi-scale plasma simulation method, and it provides a powerful and unified approach for the study of plasma physics.

PACS: 05.60.-k, 47.11.St, 47.70Nd, 52.30Ex

Key words: Unified gas-kinetic scheme, plasma, Vlasov equation, two-fluid equations, MHD equations, magnetic field reconnection.

Nomenclature

Constants

ϵ_0	Vacuum permittivity
μ_0	Vacuum permeability
c	Speed of light in vacuum
e	Charge of a proton

Characteristic variables

B_0	Characteristic strength of magnetic field
l_0	Characteristic length, plasma size
m_i	Characteristic molecular mass, ion molecular mass
n_0	Characteristic number density
U_0	Characteristic velocity, ion thermal velocity

Sup/Sub-scripts

α	Components of plasma: $\alpha = i$ stands for ion, $\alpha = e$ stands for electron
$\hat{\cdot}$	Nondimensional quantities
$\bar{\cdot}$	Averaged quantities in AAP model
i,j	Index for numerical cell and numerical cell interface

https://doi.org/10.4208/cicp.OA-2017-0102 Published online by Cambridge University Press

Variables

χ	Ratio between the electric field divergence error propagation speed and the speed of light
ℓ_α	Particle mean free path of species α
γ	Ratio between the magnetic field divergence error propagation speed and the speed of light
λ_D	Debye length
$\boldsymbol{\ell}$	Particle acceleration due to Lorenz force
$\mathbf{B}$	Magnetic field
$\mathbf{E}$	Electric field
$\mathbf{F}_\alpha$	Averaged Lorenz force on particles of species α
$\mathbf{j_e}$	Electron current density
$\mathbf{j_i}$	Ion current density
$\mathbf{j}$	Total current density
$\mathbf{W}_\alpha$	Conservative variables of species α
$\mathscr{E}_\alpha$	Total energy density of species α
$\nu_{\alpha r}$	Interspecies interaction coefficient
ν_{ee}	Collision rate of electrons
ν_{ii}	Collision rate of ions
ω_c	Cyclotron frequency
ω_p	Plasma frequency
$\overline{\mathbf{W}}_\alpha$	Averaged conservative variables in AAP model
ϕ	Artificial potential to correct electric field divergence error
ψ	Artificial potential to correct magnetic field divergence error
σ	Electric conductivity
τ_α	Relaxation parameter in BGK equation
Kn	Knudsen number
Re_m	Magnetic Reynolds number
c_m	Fast magneto-sound speed
c_s	Sound speed
f_α	Velocity distribution function of species α
r_{L_i}	Ion Larmor radius
$\lvert s_i \rvert$	Length of the i-th interface

https://doi.org/10.4208/cicp.OA-2017-0102 Published online by Cambridge University Press

1 Introduction

Generally, plasma is a medium with positive, negative, and neutral particles. It is quasi-neutral on the length scale larger than the Debye length $\lambda_D = \sqrt{\epsilon_0 k_B T_i / n_i e^2}$. The plasma concerned is the weakly coupled plasma, such as the plasma in the solar corona, the magnetosphere around the Earth, the plasma inside a Tokamak, etc. as shown in Fig. 1 [1]. The dynamics of a weakly coupled plasma can be described by kinetic equations. The number of electron inside a Debye cubic, namely the plasma parameter N_D is much larger than one (equivalently the coupling parameter $\Gamma \ll 1$). In a weakly coupled plasma, the ratio of the plasma frequency $\omega_p = \sqrt{n_i e^2 / \epsilon_0 m_i}$ to the ion collision frequency ν_{ii} is larger than one, so that the collective behavior is observed on the time scale longer than the plasma period ω_p^{-1}, and on the length scale larger than the Debye length ($\lambda_D = U_0 \omega_p^{-1}$). In this work, we propose a unified gas kinetic scheme that can be applied to the fully ionized weakly coupled plasma composed of electrons and ions.

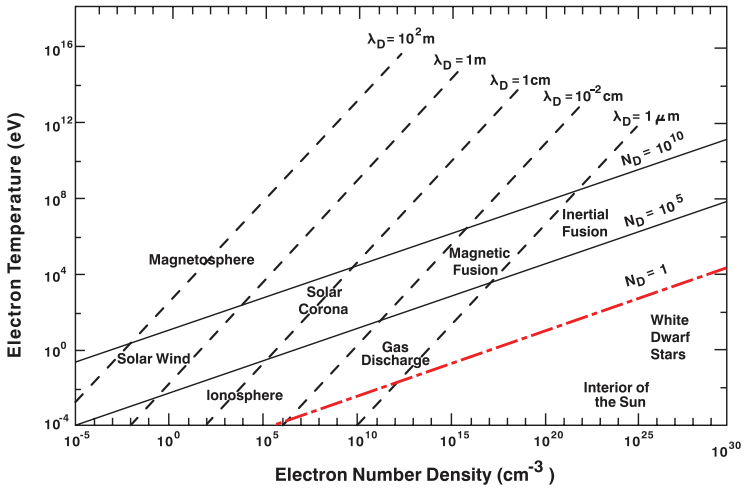


Figure 1: Diagram shows some of the range of plasma phenomena. The UGKS is mainly used for the region above the red dot-dashed line with $N_D = 1$ [1].

The motion of charged particles in a plasma is coupled with the evolution of electromagnetic field. The flow regime of a plasma is more complex than that of a neutral gas. Many plasma parameters are important in characterizing plasma flow property, such as the Debye length, the plasma frequency, the ion inertial length, and the plasma beta, etc.. Among those parameters, two parameters are important in characterizing the flow regimes of plasma, namely the Knudsen number Kn and the normalized Larmor radius $\hat{r}_{L_i}$. The Knudsen number is the ratio between the particle mean free path to a characteristic length, and the normalized Larmor radius is the ratio between the Larmor radius $r_{L_i} = m_i U_0 / eB$ and the characteristic length. The Knudsen number indicates the collision intensity and the normalized Larmor radius indicates the magnetization of

https://doi.org/10.4208/cicp.OA-2017-0102 Published online by Cambridge University Press

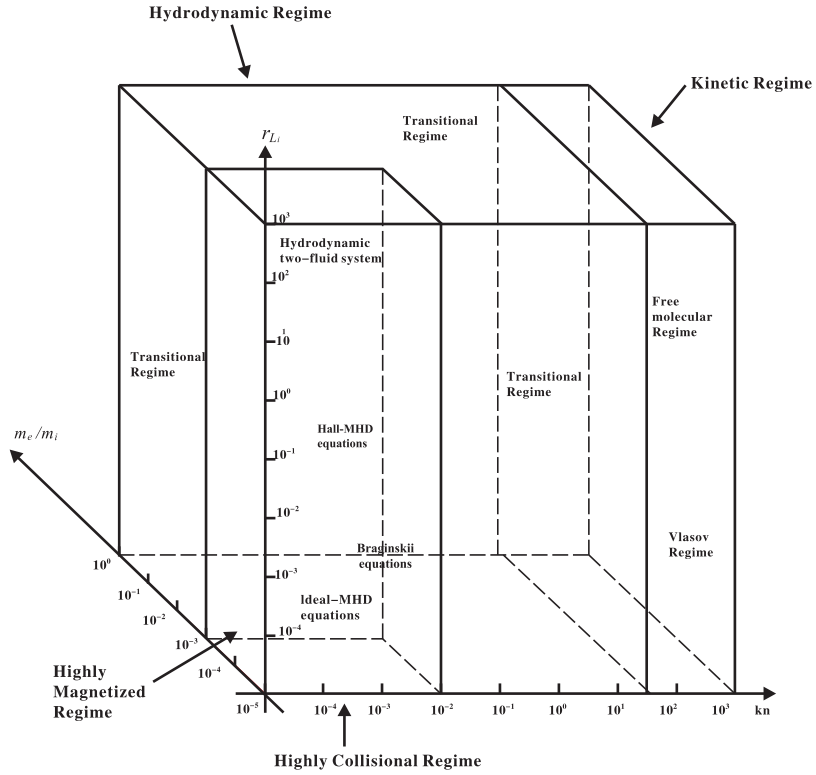


Figure 2: Flow regimes of plasma.

plasma. On the kinetic scale, the dynamics of plasma is described by kinetic equations such as the Fokker-Planck-Landau equation [2]. In the kinetic equations, the averaged electromagnetic field effect is modeled to the order of the reciprocal of the normalized Larmor radius and the collision term effect is modeled to the order of the reciprocal of the Knudsen number. Different plasma physics is shown in Fig. 2. In the rarefied regime with large Knudsen number, the plasma follows the collisionless Vlasov equation. In the highly collisional regime, the plasma is described by the hydrodynamic-type equations. When $\hat{r}_{L_i} \ll 1$, the plasma can be described by single-fluid MHD equations. The two-fluid effect or the Hall effect becomes important in the flow regimes with large $\hat{r}_{L_i}$.

Numerical methods have been developed for plasma simulation since 1950s, such as the particle-in-cell (PIC) method, the kinetic Vlasov solvers, and the hydrodynamic MHD solvers. The traditional PIC method suffers from statistical noise and restricted time step [3, 4]. In order to overcome those shortcomings, a series of asymptotic preserving PIC methods are developed by Degond *et al.* [6–8], which remain stable and consist with quasi-neutral models in the quasi-neutral limit. Reformulated Vlasov-Poisson/Maxwell equations are used in the AP-PIC methods to unify models in different regimes. A good review about AP-PIC methods and multiscale models for plasma physics was given by Degond *et al.* recently [25].

https://doi.org/10.4208/cicp.OA-2017-0102 Published online by Cambridge University Press

Based on high order phase space reconstruction techniques, many high order Vlasov solvers are proposed such as the conservative method [5], the semi-Lagrange method [9], the finite element method [10], and finite difference method [11]. The Vlasov solvers can capture solutions of the collisionless Vlasov equation accurately. However only few work has been done to study the full kinetic equation including both the electromagnetic acceleration and the collision integral term for multi-species.

In the highly collisional and highly magnetized regimes, the plasma flow is governed by the hydrodynamic-type equations. Riemann-solution-based MHD solvers [12,13] and the kinetic-based MHD solvers [14,15] have been proposed, which can recover the ideal MHD equations, and the extended Hall-MHD or dissipative MHD equations. Those methods aim to solve the single-fluid hydrodynamic equations, and hence can only be applied on the scale much larger than the Larmor radius and in the regime close to equilibrium. Another type of schemes are proposed based on the two-fluid system [16–20]. The two-fluid model takes into account the electron mass and the separation of electrons and ions, which can recover the flow regimes from MHD to Euler one.

In the transitional regime, hybrid methods are usually proposed to connect the kinetic solver with the hydrodynamic one [21,22]. In the hybrid models, the PIC method is used in the collisionless regime and the hydrodynamic models are used in the collisional regime. The main difficulty for the hybrid method is to find a proper criteria to couple different numerical models. And the solutions are not physically reliable in the transitional regime. A series of asymptotic preserving (AP) schemes have been developed for the kinetic FPL equations, which can preserve the collisionless and Euler regimes [23,24]. But currently the AP schemes are only developed for a single species flow, and therefore cannot be applied to multi-component plasma transport. Even with asymptotic preserving property, the cell size is still limited by the mean free path scale for accuracy consideration for the capturing of dissipative solution in almost all existing AP schemes.

In the past years, based on the methodology of direct modeling on the mesh size and time step scales, the UGKS has been developed to simulate multiple scale transport problems. The UGKS models the flow physics on the scale of mesh size and time step as shown in Fig. 3. When the cell size is on the hydrodynamical scale the UGKS recovers the hydrodynamic wave phenomenon, and when the cell size is on the scale less than the mean free path the UGKS recovers the particle free transport. In the transitional regime when the cell size is on the scale of mean free path, the UGKS provides a physically consistent numerical flux based on the time accurate evolution solution of kinetic equation. The UGKS connects the hydrodynamic flow physics to the kinetic particle transport seamlessly. For the rarefied gas dynamics, radiative transfer, and phonon transport, the UGKS becomes a successful multi-scale method and provides accurate solutions in all regimes [26–32].

In this paper, for the first time the UGKS is developed for the plasma simulation. The corresponding scheme is based on the space and time evolution solution of the Vlasov-BGK equations for electron and ion, and the Maxwell equations for electromagnetic field.

https://doi.org/10.4208/cicp.OA-2017-0102 Published online by Cambridge University Press

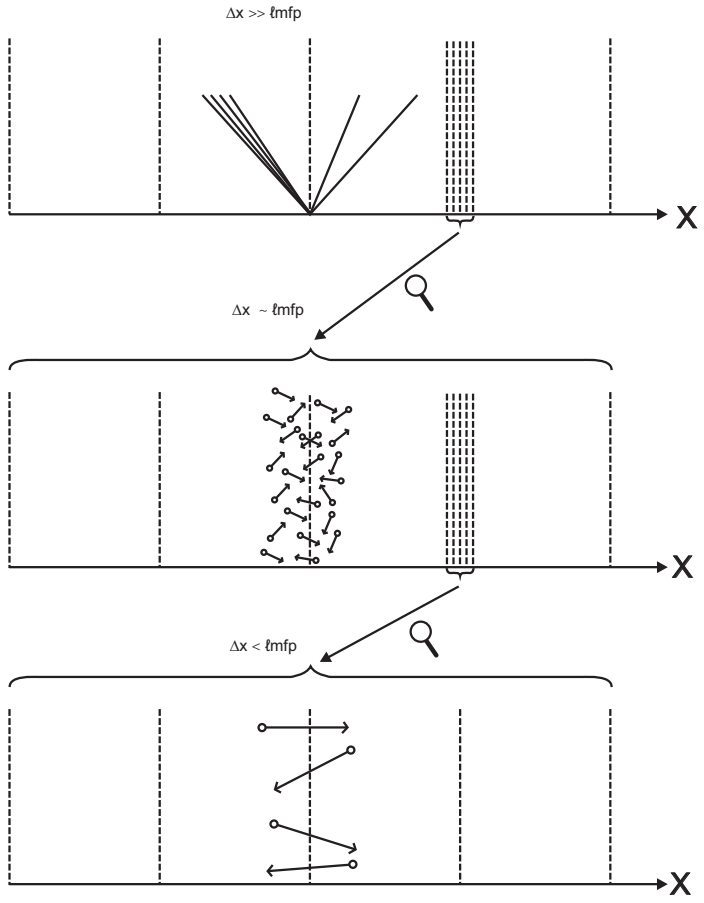


Figure 3: Multi-scale modeling in UGKS on different mesh size scale.

During this modeling process, the evolution solution on the numerical cell size and time step is used for the construction of the scheme. The coupling of the particle transport, collision, acceleration in the flux calculation, and the implicit treatment of the source terms inside each control volume, endow the scheme with multi-scale nature. With the variation of Knudsen number, inter-species collision frequency, and dimensionless Larmor radius, the scheme unifies the solutions in the kinetic Vlasov regime, the two-fluid regime, and the MHD regime with a smooth transition among them.

The outline of this paper is the following. Section 2 reviews the kinetic equations, the Maxwell equations, and their asymptotic behavior in limiting flow regimes. The detailed formulation of UGKS is proposed in Section 3. Section 4 studies the numerical property of UGKS as well as the stability constraint. The numerical test cases are given in Section 5 to validate the UGKS in different flow regimes. The last section is the conclusion.

https://doi.org/10.4208/cicp.OA-2017-0102 Published online by Cambridge University Press

2 A review of kinetic and hydrodynamic model equations of plasma

2.1 Kinetic equations and Maxwell equations

The dynamics of a fully ionized plasma are modeled by the Fokker-Planck-Landau (FPL) equations on the kinetic level

$$\frac{\partial f_\alpha}{\partial t}+\mathbf{u}\cdot\nabla_{\mathbf{x}}f_\alpha+\frac{\mathbf{F}_\alpha}{m_\alpha}\cdot\nabla_{\mathbf{u}}f_\alpha=\sum_\beta Q_{\alpha,\beta}(f_\alpha,f_\beta), \tag{2.1}$$

where $f_\alpha(\mathbf{x},t,\mathbf{u})$ is the velocity distribution function of species α ($\alpha=i$ for ion and $\alpha=e$ for electron). The conservative variables $\mathbf{W}_\alpha$ can be calculated by taking the conservative moments of f_α

$$\mathbf{W}_\alpha=\int\Psi f_\alpha d\mathbf{u}, \tag{2.2}$$

where $\Psi=\left(1,u,v,w,\frac{1}{2}(u^2+v^2+w^2)\right)^T$. $\mathbf{F}_\alpha=e(\mathbf{E}+\mathbf{u}_\alpha\times\mathbf{B})$ is the averaged electromagnetic force. The collision term $Q_{\alpha,\beta}(f_\alpha,f_\beta)$ describes the binary collisions between charged particles with long-range Coulomb interactions

$$Q_{\alpha,\beta}(f_\alpha,f_\beta)=\nabla_{\mathbf{u}}\cdot\left(\int_{\mathbb{R}^3}\Phi(\mathbf{u}-\mathbf{u}')(\nabla_{\mathbf{u}}f_\alpha f'_\beta-\nabla'_{\mathbf{u}}f'_\beta f_\alpha)d\mathbf{u}'\right), \tag{2.3}$$

where $\Phi(\mathbf{u})$ is a 3×3 matrix

$$\Phi(\mathbf{u})=\frac{1}{|\mathbf{u}|^3}(|\mathbf{u}|^2I_3-\mathbf{u}\otimes\mathbf{u}).$$

In this work, in order to avoid the complexity and high computational cost of the nonlinear Landau collision term, a single BGK-type collision operator proposed by Andries, Aoki, and Perthame (AAP model) is employed to model the collision process [33]. The Landau collision operator can be built into our scheme as well using the method we proposed for Boltzmann collision operator [35]. In AAP model, one global collision operator is used for each component to take into account of both self-collision and cross-collision, and the kinetic equations read

$$\frac{\partial f_\alpha}{\partial t}+\mathbf{u}\cdot\nabla_{\mathbf{x}}f_\alpha+\frac{\mathbf{F}_\alpha}{m_\alpha}\cdot\nabla_{\mathbf{u}}f_\alpha=\frac{f_\alpha^+-f_\alpha}{\tau_\alpha}, \tag{2.4}$$

where post collision distribution f_α^+ is a Maxwellian distribution

$$f_\alpha^+=\rho_\alpha\left(\frac{m_\alpha}{2\pi k_B\overline{T}_\alpha}\right)^{3/2}\exp\left(-\frac{m_\alpha}{2\pi k_B\overline{T}_\alpha}(u-\overline{\mathbf{U}}_\alpha)^2\right). \tag{2.5}$$

https://doi.org/10.4208/cicp.OA-2017-0102 Published online by Cambridge University Press

The parameters $\overline{T}_\alpha$ and $\overline{\mathbf{U}}_\alpha$ are connected to the macroscopic properties of individual components by [33]

$$\begin{aligned}\overline{\mathbf{U}}_\alpha &= \mathbf{U}_\alpha + \tau_\alpha \sum_r 2\frac{m_r}{m_\alpha+m_r}\nu_{\alpha r}(\mathbf{U}_r-\mathbf{U}_\alpha),\\ \frac{3}{2}k_B\overline{T}_\alpha &= \frac{3}{2}k_BT_\alpha - \frac{m_\alpha}{2}(\overline{\mathbf{U}}_\alpha-\mathbf{U}_\alpha)^2\\ &\quad + \tau_\alpha\sum_r 4m_\alpha\frac{m_r}{(m_\alpha+m_r)^2}\nu_{\alpha r}\left(\frac{3}{2}k_BT_r-\frac{3}{2}k_BT_\alpha+\frac{m_r}{2}(\mathbf{U}_r-\mathbf{U}_\alpha)^2\right),\end{aligned} \tag{2.6}$$

where $\nu_{\alpha r}$ are the interaction coefficients that measure the strength of intermolecular collision. The relaxation time is determined by $\tau_\alpha = 1/\sum_r \nu_{\alpha r}$. The parameter ν_{α_r} is determined by molecular models, and the hard sphere model is used in this paper [34].

The averaged electric field $\mathbf{E}$ and magnetic field $\mathbf{B}$ follow the Maxwell equations,

$$\begin{cases}\dfrac{\partial \mathbf{B}}{\partial t} = -\nabla_{\mathbf{x}}\times\mathbf{E},\\ \dfrac{\partial \mathbf{E}}{\partial t} = c^2\nabla_{\mathbf{x}}\times\mathbf{B}-\dfrac{1}{\epsilon_0}\mathbf{j},\end{cases} \tag{2.7}$$

where c is the speed of light, ϵ_0 is the vacuum permittivity which is related to the vacuum permeability ν_0 by $c=(\nu_0\epsilon_0)^{-1/2}$. The electromagnetic field satisfies the divergence constraints

$$\nabla_{\mathbf{x}}\cdot\mathbf{E} = \frac{e}{\epsilon_0}(n_i-n_e), \qquad \nabla_{\mathbf{x}}\cdot\mathbf{B}=0, \tag{2.8}$$

where e is the charge of a proton. Theoretically, the divergence constraints will always hold if they are initially satisfied. However numerical techniques are needed to make sure that the divergence constraints are satisfied by numerical solutions. The perfectly hyperbolic Maxwell equations (PHM) [36] are used in current work to evolve the electromagnetic field which preserve the divergence constraints,

$$\begin{aligned}&\frac{\partial \mathbf{E}}{\partial t} - c^2\nabla_{\mathbf{x}}\times\mathbf{B} + \chi c^2\nabla_{\mathbf{x}}\phi = -\frac{1}{\epsilon_0}\mathbf{j},\\ &\frac{\partial \mathbf{B}}{\partial t} + \nabla_{\mathbf{x}}\times\mathbf{E} + \gamma\nabla_{\mathbf{x}}\psi = 0,\\ &\frac{1}{\chi}\frac{\partial \phi}{\partial t} + \nabla_{\mathbf{x}}\cdot\mathbf{E} = \frac{e}{\epsilon_0}(n_i-n_e),\\ &\frac{\epsilon_0\mu_0}{\gamma}\frac{\partial \psi}{\partial t} + \nabla_{\mathbf{x}}\cdot\mathbf{B} = 0,\end{aligned} \tag{2.9}$$

where $\mathbf{j}$ is the total electric current density $\mathbf{j} = en_i\mathbf{U}_i - en_e\mathbf{U}_e$, ϕ, ψ are artificial correction potentials. Munz *et al.* proved that the propagation speed of magnetic field divergence error and electric field divergence error are γc and χc [36]. Our scheme is built on the BGK-Maxwell system Eqs. (2.4), (2.7), (2.8), which are able to cover the flow regimes of plasma from the collisionless Vlasov regime to the continuum MHD regime.

https://doi.org/10.4208/cicp.OA-2017-0102 Published online by Cambridge University Press

2.2 Asymptotic limits of BGK-Maxwell system

The BGK-Maxwell system is nondimensionalized by the characteristic length l_0 (plasma size) and characteristic velocity $U_0=\sqrt{k_BT_0/m_i}$ (ion thermal speed), which produce the characteristic time of l_0/U_0. The characteristic molecule mass is ion mass m_i, and the characteristic number density n_0, which produce the characteristic energy density $m_in_0U_0^2$, and the characteristic velocity distribution m_in_0/U_0^3. The electric field is normalized by the product of the characteristic magnetic field B_0 and characteristic velocity, i.e., $E_0=B_0U_0$,

$$\begin{aligned}&\hat{x}=\frac{x}{l_0},\quad \hat{\mathbf{u}}=\frac{\mathbf{u}}{u_0},\quad \hat{t}=\frac{u_0}{l_0}t,\quad \hat{m}=\frac{m}{m_i},\quad \hat{n}_\alpha=\frac{n_\alpha}{n_0},\quad \hat{E}=\frac{E}{m_in_0U_0^2},\\&\hat{f}\alpha=\frac{U_0^3}{m_in_0}f_\alpha,\quad \hat{\mathbf{B}}=\frac{\mathbf{B}}{B_0},\quad \hat{\mathbf{E}}=\frac{\mathbf{E}}{B_0U_0},\quad \hat{\mathbf{j}}=\frac{\mathbf{j}}{en_0U_0},\quad \hat{\lambda}_D=\frac{\lambda_D}{r_{L_i}}.\end{aligned}\tag{2.10}$$

In the following of this paper, all variables are nondimensionalized, and the hats are omitted for simplicity. Inserting the normalized variables into the BGK-Maxwell system, we get the following scaled BGK-Maxwell system

$$\begin{aligned}&\frac{\partial f_\alpha}{\partial t}+\mathbf{u}\cdot\nabla_{\mathbf{x}}f_\alpha+\frac{1}{r_{L_i}m_\alpha}(\mathbf{E}+\mathbf{u}\times\mathbf{B})\cdot\nabla_{\mathbf{u}}f_\alpha=\frac{f_\alpha^+-f_\alpha}{\tau_\alpha},\\&\frac{\partial\mathbf{B}}{\partial t}+\nabla_{\mathbf{x}}\times\mathbf{E}=0,\\&\frac{\partial\mathbf{E}}{\partial t}-c^2\nabla_{\mathbf{x}}\times\mathbf{B}=-\frac{1}{\lambda_D^2r_{L_i}}\mathbf{j},\end{aligned}\tag{2.11}$$

where the divergence constraints for electromagnetic fields are

$$\nabla_{\mathbf{x}}\cdot\mathbf{E}=\frac{n_i-n_e}{\lambda_D^2r_{L_i}},\quad \nabla_{\mathbf{x}}\cdot\mathbf{B}=0.\tag{2.12}$$

The physically significant similarity parameters are: normalized relaxation time τ_α, the scaled Debye length λ_D, the normalized ion Larmor radius r_{L_i}, the normalized speed of light c, and the normalized electron mass m_e in the non-dimensional equations. In the following, we briefly review the asymptotic limits of the BGK-Maxwell system with respect to these similarity parameters, and the detailed derivations are presented in Appendix A.

The normalized relaxation time τ_α is proportional to the Knudsen number Kn_α, which is defined as the ratio between the mean free path ℓ_α and the length scale l_0. When $\tau_\alpha\ll\min(1,\nu_{ie}^{-1})$, the first order of the BGK-Maxwell system with respect to τ_α gives the

https://doi.org/10.4208/cicp.OA-2017-0102 Published online by Cambridge University Press

following hydrodynamic two-fluid Navier-Stokes equations

$$\begin{aligned}
&\partial_t \rho_\alpha + \nabla_{\mathbf{x}} \cdot (\rho_\alpha \mathbf{U}_\alpha) = 0, \\
&\partial_t (\rho_\alpha \mathbf{U}_\alpha) + \nabla_{\mathbf{x}} \cdot (\rho_\alpha \mathbf{U}_\alpha \mathbf{U}_\alpha + p_\alpha \mathbb{I} - \mu\sigma(\mathbf{U}_\alpha)) = \frac{n_\alpha}{r_{L_i}} (\mathbf{E} + \mathbf{U}_\alpha \times \mathbf{B}) + S_\alpha, \\
&\partial_t \mathscr{E}_\alpha + \nabla_{\mathbf{x}} \cdot ((\mathscr{E}_\alpha + p_\alpha)\mathbf{U}_\alpha - \mu\sigma(\mathbf{U}_\alpha)\mathbf{U} + \kappa \nabla_x T) = \frac{n_\alpha}{r_{L_i}} \mathbf{U}_\alpha \cdot \mathbf{E} + Q_\alpha,
\end{aligned} \tag{2.13}$$

where the tensor $\sigma(\mathbf{U})$ denotes the strain rate tensor given by

$$\sigma(\mathbf{U}_\alpha) = \left(\nabla_x \mathbf{U}_\alpha + (\nabla_x \mathbf{U}_\alpha)^T \right) - \frac{2}{3} \mathrm{div}_x \mathbf{U}_\alpha \mathbb{I}. \tag{2.14}$$

The viscosity μ_α and the thermal conductivity κ_α can be expressed by the relaxation parameter τ_α as

$$\mu_\alpha = \tau_\alpha n_\alpha k_B T_\alpha, \quad \kappa_\alpha = \tau_\alpha \frac{5}{2} \frac{k_B}{m} n k_B T. \tag{2.15}$$

In the two-fluid system, $S_i = -S_e$ and $Q_i = -Q_e$ are the corresponding momentum and energy exchange between electron and ion,

$$\begin{aligned}
S_\alpha &= \int \mathbf{u} \frac{f_\alpha^+ - f_\alpha}{\tau_\alpha} d\mathbf{u} = \sum_r \frac{2 m_\alpha m_r}{m_\alpha + m_r} n_\alpha \nu_{\alpha r} (\mathbf{U}_r - \mathbf{U}_\alpha), \\
Q_\alpha &= \int \frac{1}{2} |\mathbf{u} - \mathbf{U}|^2 \frac{f_\alpha^+ - f_\alpha}{\tau_\alpha} d\mathbf{u} \\
&= \sum_r \frac{4 m_\alpha m_r}{(m_\alpha + m_r)^2} n_r \nu_{\alpha r} \left(\frac{3}{2} k_B T_r - \frac{3}{2} k_B T_\alpha + \frac{m_r}{2} (\mathbf{U}_r - \mathbf{U}_\alpha)^2 \right).
\end{aligned} \tag{2.16}$$

In the non-conductive limit where the interspecies molecular interaction is intensive and the electromagnetic waves cannot penetrate, i.e. $\nu_{ie}^{-1} \ll \min(1, r_{L_i})$, the zero-th order of the two-fluid system with respect to τ_α and $(r_{L_i} \nu_{ie})^{-1}$ gives the Euler equations for common velocity $\mathbf{U} = \mathbf{U}_i = \mathbf{U}_e$ and common temperature $T = T_i = T_e$,

$$\begin{aligned}
&\partial_t \rho_\alpha + \nabla_{\mathbf{x}} \cdot (\rho_\alpha \mathbf{U}) = 0, \\
&\partial_t (\rho \mathbf{U}) + \nabla_{\mathbf{x}} \cdot (n k_B T I + \rho \mathbf{U}\mathbf{U}) = 0, \\
&\partial_t \mathscr{E} + \nabla_{\mathbf{x}} \cdot ((\mathscr{E} + n k_B T)\mathbf{U}) = 0,
\end{aligned} \tag{2.17}$$

where

$$\mathscr{E} = \frac{3}{2} n k_B T + \frac{\rho}{2} \mathbf{U}^2 = \sum_\alpha \mathscr{E}_\alpha, \tag{2.18}$$

with $\mathscr{E}_\alpha$ the total energy density of species α. In the flow regime where $m_e \ll m_i$, $\lambda_D \sim c^{-1} \ll 1$ with a modest value of ν_{ie}, the first order with respect to r_{L_i}, the zero-th order

https://doi.org/10.4208/cicp.OA-2017-0102 Published online by Cambridge University Press

with respect of τ_α, m_e/m_i and λ_D of the two-fluid system give the Hall-MHD equations,

$$\begin{aligned}
&\partial_t\rho+\nabla_{\mathbf{x}}\cdot(\rho\mathbf{U})=0,\\
&\partial_t(\rho\mathbf{U})+\nabla_{\mathbf{x}}\cdot(\rho\mathbf{U}\mathbf{U}+p_i\mathbf{I})=\frac{\rho_i}{m_i r_{L_i}}(\mathbf{E}+\mathbf{U}\times\mathbf{B}),\\
&\mathbf{E}+\mathbf{U}\times\mathbf{B}=\frac{r_{L_i}}{\sigma}\mathbf{j}+\frac{1}{n_e e}\mathbf{j}\times\mathbf{B}+\frac{r_{L_i}}{n_e e}\nabla_{\mathbf{x}}p_e,\\
&\partial_t\mathscr{E}_\alpha+\nabla_{\mathbf{x}}\cdot((\mathscr{E}_\alpha+p_\alpha)\mathbf{U}_\alpha)=\frac{1}{r_{L_i}}\mathbf{j}_\alpha\cdot\mathbf{E},\\
&\partial_t\mathbf{B}+\nabla_{\mathbf{x}}\times\mathbf{E}=0,\\
&\mathbf{j}=r_{L_i}\lambda_D^2c^2\nabla_{\mathbf{x}}\times\mathbf{B},
\end{aligned}\tag{2.19}$$

where $\rho=\rho_i+\rho_e$ is the total density, and $\mathbf{j}_e=-n_e e\mathbf{U}_e$ is electron current density, $\mathbf{j}_i=n_i e\mathbf{U}_i$ is ion current density, and

$$\sigma=\frac{n_i e^2(m_i+m_e)}{2m_i m_e\nu_{ie}}\approx\frac{n_i e^2}{2m_e\nu_{ie}}$$

is the electrical conductivity, which is related to the magnetic Reynolds number Re_m by $\sigma=\mathrm{Re}_m\lambda_D^2r_{L_i}^2c^2$.

The ideal-MHD equations are the zero-th order approximation of the MHD equations (2.19) with respect to the Larmor radius, which read

$$\begin{aligned}
&\partial_t\rho+\nabla_{\mathbf{x}}\cdot(\rho\mathbf{U})=0,\\
&\partial_t(\rho\mathbf{U})+\nabla_{\mathbf{x}}\cdot(\rho\mathbf{U}\mathbf{U}+pI)=\frac{(\mathbf{B}\cdot\nabla_{\mathbf{x}})\mathbf{B}}{\mu_0}-\nabla_{\mathbf{x}}\left(\frac{\mathbf{B}^2}{2\mu_0}\right),\\
&\partial_t\mathscr{E}+\nabla_{\mathbf{x}}\cdot((\mathscr{E}+p)\mathbf{U})=\frac{1}{\mu_0}\rho\mathbf{U}\cdot(\nabla_{\mathbf{x}}\times\mathbf{B}\times\mathbf{B}),\\
&\partial_t\mathbf{B}+\nabla_{\mathbf{x}}\times(\mathbf{U}\times\mathbf{B})=0,
\end{aligned}\tag{2.20}$$

where $p=p_i+p_e$ is the total pressure, $(\mathbf{B}\cdot\nabla_{\mathbf{x}})\mathbf{B}/\mu_0$ is the magnetic tension force, and $\nabla_{\mathbf{x}}(\mathbf{B}^2/2\mu_0)$ is magnetic pressure.

The above analysis shows that in the continuum regime, when the interspecies collisions are strong, the gas mixture behaves like dielectric material, and the BGK-Maxwell equations goes to Euler equations Eq. (2.17). For a conductive plasma, the BGK-Maxwell equations can span the complete range from the neutral two-fluid system to the resistive-MHD, Hall-MHD, and ideal MHD equations as shown in Fig. 4. The developed UGKS can be applied in the transition regime as well with modest Knudsen number, Debye length, and Larmor radius, where the corresponding macroscopic governing equations are not well defined.

https://doi.org/10.4208/cicp.OA-2017-0102 Published online by Cambridge University Press

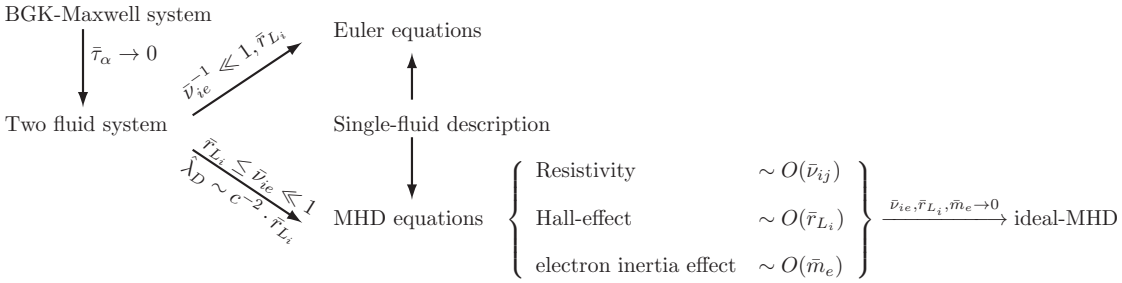


Figure 4: Asymptotic limits of BGK-Maxwell system.

3 Unified gas kinetic scheme

3.1 General framework

The UGKS is a finite volume scheme for the time evolution of both microscopic distribution function in the phase space $\mathbf{X} = \sum_i \Omega_{\mathbf{x}i} \otimes \sum_j \Omega_{\mathbf{u}j} = \sum_{i,j} \Omega_{\mathbf{x}i \times \mathbf{u}j}$, and the macroscopic variables in the physical space $\sum_i \Omega_{\mathbf{x}i}$. The averaged macroscopic conservative variables in a physical cell $\Omega_{\mathbf{x}i}$ are

$$(\mathbf{W}_\alpha)_i = \frac{1}{|\Omega_{\mathbf{x}i}|} \int_{\Omega_{\mathbf{x}i}} \mathbf{W}_\alpha d\mathbf{x},$$

similar for the cell averaged electromagnetic field and divergence correction terms $\mathbf{Q}_i = (E_{1i}, E_{2i}, E_{3i}, B_{1i}, B_{2i}, B_{3i}, \phi_i, \psi_i)^T$. The averaged distribution function in a phase space cell $\Omega_{\mathbf{x}i \times \mathbf{u}j}$ is

$$(f_\alpha)_{ij} = \frac{1}{|\Omega_{\mathbf{x}i \times \mathbf{u}j}|} \int_{\Omega_{\mathbf{x}i \times \mathbf{v}j}} f_\alpha d\mathbf{x} d\mathbf{u}.$$

The time evolution of the velocity distribution function

$$(f_\alpha)_{ij}^{n+1} = (f_\alpha)_{ij}^n - \frac{1}{|\Omega_{\mathbf{x}i}|} \sum_{s_i \in \partial_{\Omega_{\mathbf{x}i}}} |s_i| \mathscr{F}^x_{f_\alpha s_i} - \frac{1}{|\Omega_{\mathbf{u}j}|} \sum_{s_j \in \partial_{\Omega_{\mathbf{u}j}}} |s_j| \mathscr{F}^v_{f_\alpha s_j} + \int_{t^n}^{t^{n+1}} \frac{f^+_{\alpha ij} - f_{\alpha ij}}{\tau_\alpha} dt, \tag{3.1}$$

is coupled with the time evolution of the conservative variables

$$(\mathbf{W}_\alpha)_i^{n+1} = (\mathbf{W}_\alpha)_i^n - \frac{1}{|\Omega_{\mathbf{x}i}|} \sum_{s_i \in \partial \Omega_{\mathbf{x}i}} |s_i| \mathscr{F}_{\mathbf{W}_\alpha s_i} + \frac{\Delta t}{\tau_\alpha} \left((\bar{\mathbf{W}})_i^n - (\mathbf{W}_\alpha)_i^n \right) + \Delta t \mathbf{S}^{n+1}_{\mathbf{W}_\alpha i}, \tag{3.2}$$

https://doi.org/10.4208/cicp.OA-2017-0102 Published online by Cambridge University Press

where $\overline{\mathbf{W}}=(\rho_\alpha,\rho_\alpha\overline{\mathbf{U}}_\alpha,\rho_\alpha\overline{\mathscr{E}}_\alpha)^T$, and $\overline{\mathbf{U}}_\alpha$ and $\overline{\mathscr{E}}_\alpha$ are the averaged quantities in AAP model as Eq. (2.6). More specifically, the componentwise macroscopic equations are

$$(\boldsymbol{\rho}_\alpha)_i^{n+1}=(\boldsymbol{\rho}_\alpha)_i^n-\frac{1}{|\Omega_{\mathbf{x}i}|}\sum_{s_i\in\partial\Omega_{\mathbf{x}i}}|s_i|\int_{t^n}^{t^{n+1}}\int\mathbf{u}\cdot\mathbf{n}_{s_i}f_\alpha(\mathbf{x}_{s_i},t,\mathbf{u})d\mathbf{u}dt, \tag{3.3}$$

$$\begin{aligned}(\boldsymbol{\rho}_\alpha\mathbf{U}_\alpha)_i^{n+1}=&(\boldsymbol{\rho}_\alpha\mathbf{U}_\alpha)_i^n-\frac{1}{|\Omega_{\mathbf{x}i}|}\sum_{s_i\in\partial\Omega_{\mathbf{x}i}}|s_i|\int_{t^n}^{t^{n+1}}\int(\mathbf{u}\cdot\mathbf{n}_{s_i})\mathbf{u}f_\alpha(\mathbf{x}_{s_i},t,\mathbf{u})d\mathbf{u}dt\\&+\frac{\Delta t}{\tau_\alpha}(\rho_\alpha^n\overline{\mathbf{U}^n}_\alpha-\rho_\alpha^n\mathbf{U}_\alpha^n)+\frac{\Delta t}{r_{L_i}}n_\alpha^{n+1}(\mathbf{E}^{n+1}+\mathbf{U}_\alpha^{n+1}\times\mathbf{B}^{n+1}),\end{aligned} \tag{3.4}$$

$$\begin{aligned}(\boldsymbol{\rho}_\alpha\mathscr{E}_\alpha)_i^{n+1}=&(\boldsymbol{\rho}_\alpha\mathscr{E}_\alpha)_i^n-\frac{1}{|\Omega_{\mathbf{x}i}|}\sum_{s_i\in\partial\Omega_{\mathbf{x}i}}|s_i|\int_{t^n}^{t^{n+1}}\int(\mathbf{u}\cdot\mathbf{n}_{s_i})\frac{\mathbf{u}^2}{2}f_\alpha(\mathbf{x}_{s_i},t,\mathbf{u})d\mathbf{u}dt\\&+\frac{\Delta t}{\tau_\alpha}(\rho_\alpha^n\overline{\mathscr{E}^n}_\alpha-\rho_\alpha^n\mathscr{E}_\alpha^n)+\frac{\Delta t}{r_{L_i}}n_\alpha^{n+1}\mathbf{U}_\alpha^{n+1}\cdot\mathbf{E}^{n+1}.\end{aligned} \tag{3.5}$$

The time evolution of the electromagnetic fields is

$$\mathbf{Q}_i^{n+1}=\mathbf{Q}_i^n+\frac{\Delta t}{|\Omega_{\mathbf{x}i}|}\sum_{s_i\in\partial\Omega_{\mathbf{x}i}}|s_i|\mathscr{F}_{\mathbf{Q}s_i}+\Delta t\mathbf{S}_{Q_i}^{n+1}, \tag{3.6}$$

which include the equations

$$\mathbf{E}_i^{n+1}=\mathbf{E}_i^n+\frac{\Delta t}{|\Omega_{\mathbf{x}i}|}\sum_{s_i\in\partial\Omega_{\mathbf{x}i}}|s_i|\mathscr{F}_{\mathbf{E}s_i}-\frac{\Delta t}{\lambda_D r_{L_i}}(n_i^{n+1}\mathbf{U}_i^{n+1}-n_e^{n+1}\mathbf{U}_e^{n+1}), \tag{3.7}$$

$$\mathbf{B}_i^{n+1}=\mathbf{B}_i^n+\frac{\Delta t}{|\Omega_{\mathbf{x}i}|}\sum_{s_i\in\partial\Omega_{\mathbf{x}i}}|s_i|\mathscr{F}_{\mathbf{B}s_i}, \tag{3.8}$$

$$\phi_i^{n+1}=\phi_i^n+\frac{\Delta t}{|\Omega_{\mathbf{x}i}|}\sum_{s_i\in\partial\Omega_{\mathbf{x}i}}|s_i|\mathscr{F}_{\phi s_i}+\frac{\Delta t\chi}{\lambda_D r_{L_i}}(n_i^{n+1}-n_e^{n+1}), \tag{3.9}$$

$$\psi_i^{n+1}=\psi_i^n+\frac{\Delta t}{|\Omega_{\mathbf{x}i}|}\sum_{s_i\in\partial\Omega_{\mathbf{x}i}}|s_i|\mathscr{F}_{\psi s_i}, \tag{3.10}$$

where $|\Omega_{\mathbf{x}i}|$ is the volume of the cell, $s_i\in\partial\Omega_{\mathbf{x}i}$ is the cell interface, and $|s_i|$ is the length of the i-th cell interface. The numerical fluxes in UGKS for the distribution function and conservative variables are calculated from a time-dependent distribution function $f_\alpha(\mathbf{x}_{s_i},t,\mathbf{u})$, which will be presented in the next subsection, such as

$$\mathscr{F}_{f_\alpha s_i}^x=\int_{t^n}^{t^{n+1}}\mathbf{u}\cdot\mathbf{n}_{s_i}f_\alpha(\mathbf{x}_{s_i},t,\mathbf{u})dt, \tag{3.11}$$

$$\mathscr{F}_{\mathbf{W}_\alpha s_i}=\int_{t^n}^{t^{n+1}}\int\Psi\mathbf{u}\cdot\mathbf{n}_{s_i}f_\alpha(\mathbf{x}_{s_i},t,\mathbf{u})d\mathbf{u}dt, \tag{3.12}$$

$$\mathscr{F}_{f_\alpha s_j}^v=\int_{t^n}^{t^{n+1}}\boldsymbol{\ell}\cdot\mathbf{n}_{s_j}f(\mathbf{x},t,\mathbf{u}_{s_j})dt, \tag{3.13}$$

https://doi.org/10.4208/cicp.OA-2017-0102 Published online by Cambridge University Press

where $\mathbf{n}$ is the outer normal direction at interface, $\Psi=\left(1,u,v,w,\frac{1}{2}(u^2+v^2+w^2)\right)^T$, and $\boldsymbol{\ell}=(l_u,l_v,l_w)^T$ is the acceleration due to Lorenz force.

3.2 Numerical fluxes in UGKS

In this subsection, the detailed formulation of numerical flux is derived (subscript α is dropped for simplicity). The time dependent distribution function at a cell interface plays an important role in UGKS for flux calculation, which is modeled based on the integral solution of the kinetic equation Eq. (2.4),

$$f(\mathbf{x},t,\mathbf{u})=\frac{1}{\tau}\int_{t^n}^{t}f^+(\mathbf{x}',t',\mathbf{u}')\mathrm{e}^{-\frac{t-t'}{\tau}}dt'+\mathrm{e}^{-\frac{t-t^n}{\tau}}f_0(\mathbf{x}-\mathbf{u}(t-t^n),\mathbf{u}-\boldsymbol{\ell}(t-t^n)), \tag{3.14}$$

where $\mathbf{x}'=\mathbf{x}-\mathbf{u}(t-t^n-t')$, $\mathbf{u}'=\mathbf{u}-\boldsymbol{\ell}(t-t^n-t')$, and $f_0(\mathbf{x},\mathbf{u})$ is the initial distribution function at $t=t^n$. Assume that the cell interface is located at $\mathbf{x}_0$, the velocity cell center is located at $\mathbf{u}_k$, with the normal direction $\mathbf{e}_1$, and the local basis $(\mathbf{e}_1,\mathbf{e}_2,\mathbf{e}_3)$. The initial distribution function is reconstructed as

$$\begin{aligned}f_0(\mathbf{x},\mathbf{u})=&\left(f_0^L(x_0)+\Delta\mathbf{x}\cdot\frac{\partial f_0^L}{\partial\mathbf{x}}+\Delta\mathbf{u}\cdot\frac{\partial f_0^L}{\partial\mathbf{u}}\right)(1-H[\Delta\mathbf{x}\cdot\mathbf{e}_1])\\&+\left(f_0^R(\mathbf{x}_0)+\Delta\mathbf{x}\frac{\partial f_0^R}{\partial\mathbf{x}}+\Delta\mathbf{u}\cdot\frac{\partial f_0^R}{\partial\mathbf{u}}\right)H[\Delta\mathbf{x}\cdot\mathbf{e}_1],\end{aligned} \tag{3.15}$$

where $\Delta\mathbf{x}=\mathbf{x}-\mathbf{x}_0$, $\Delta\mathbf{u}=\mathbf{u}-\mathbf{u}_k$, $H[x]$ is the Heaviside function

$$H[x]=\begin{cases}1, & x>0,\\ 0, & x\le 0.\end{cases} \tag{3.16}$$

Slope limit, such as the van-Leer limiter, is used to reconstruct the slope $\partial_{\mathbf{x}}f_0$ and $\partial_{\mathbf{u}}f_0$ in each phase space cell.

The post collision distribution function is expanded around the cell interface as

$$\begin{aligned}&f^+(\mathbf{x},t,\mathbf{u})=f_0^+(\mathbf{x}_0,t,\mathbf{u})\left[1+(1-H[\tilde{x}])a^L\tilde{x}+H[\tilde{x}]a^R\tilde{x}+b\tilde{y}+c\tilde{z}+A(t-t^n)\right]\\&=f_0^+(\mathbf{x}_0,t,\mathbf{u}_k)\left[1-2\lambda(\mathbf{u}-\tilde{\mathbf{U}})\cdot\Delta\mathbf{u}\right]\left[1+(1-H[\tilde{x}])a^L\tilde{x}+H[\tilde{x}]a^R\tilde{x}+b\tilde{y}+c\tilde{z}+A(t-t^n)\right]\\&=f_0^+(\mathbf{x}_0,t,\mathbf{u}_k)\left[1-2\lambda(\mathbf{u}-\tilde{\mathbf{U}})\cdot\Delta\mathbf{u}+(1-H[\tilde{x}])a^L\tilde{x}+H[\tilde{x}]a^R\tilde{x}+b\tilde{y}+c\tilde{z}+A(t-t^n)\right],\end{aligned} \tag{3.17}$$

where $\tilde{x}=\Delta\mathbf{x}\cdot\mathbf{e}_1$, $\tilde{y}=\Delta\mathbf{y}\cdot\mathbf{e}_2$, $\tilde{z}=\Delta\mathbf{x}\cdot\mathbf{e}_3$. The coefficients $a^{L,R},b,c,A$ are related to the spatial and time derivatives of f^+, for example

$$a^{L,R}=\frac{1}{f_0^+}\frac{\partial f_0^+}{\partial\mathbf{W}_0}\frac{\partial\mathbf{W}_0^{L,R}}{\partial x}\bigg|_{x=x_0},\quad A=\frac{1}{f_0^+}\frac{\partial f_0^+}{\partial\mathbf{W}_0}\frac{\partial\mathbf{W}_0^{L,R}}{\partial t}\bigg|_{t=t^n}, \tag{3.18}$$

https://doi.org/10.4208/cicp.OA-2017-0102 Published online by Cambridge University Press

and an analogous expression can be derived for b, c. From the reconstructed distribution $f_0(\mathbf{x}_0,\mathbf{u})$, the macroscopic conservative variables at a cell interface can be calculated

$$\mathbf{W}_0(\mathbf{x}_0)=\int\Psi\left(f_0^L(\mathbf{x}_0)H[\mathbf{u}\cdot\mathbf{e}_1]+f_0^R(\mathbf{x}_0)(1-H[\mathbf{u}\cdot\mathbf{e}_1])\right)d\mathbf{u}. \tag{3.19}$$

Then, the averaged macroscopic variables $\overline{\mathbf{W}}_0$ in Eq. (2.6) can be evaluated, and its spacial derivative is reconstructed to be

$$\left.\frac{\partial\overline{\mathbf{W}}_0^{L,R}}{\partial\tilde{x}}\right|_{\mathbf{x}=\mathbf{x}_0}=\frac{\overline{\mathbf{W}}_0^{L,R}(\mathbf{x}_0)-\overline{\mathbf{W}}_0(\mathbf{x}_{L,R})}{(\mathbf{x}_0-\mathbf{x}_{L,R})\cdot\mathbf{n}}. \tag{3.20}$$

The time derivative are calculated by

$$\frac{\partial\overline{\mathbf{W}}_0}{\partial t}=\int\left((a_x^lH[u]+a_x^r(1-H[u])uf_0^++a_yvf_0^++(\mathbf{E}+\mathbf{u}\times\mathbf{B})\cdot\frac{\partial f_0^+}{\partial\mathbf{u}}\right)\Psi d\mathbf{u}. \tag{3.21}$$

Substituting Eq. (3.15) and Eq. (3.17) into the integral solution Eq. (3.14), the time dependent distribution at the cell interface is

$$\begin{aligned}
f(\mathbf{x}_0,t,\mathbf{u}_0)=&\left(1-\mathrm{e}^{(t-t^n)/\tau}\right)f_0^+(\mathbf{x}_0)\\
&+\left((t-t^n+\tau)\mathrm{e}^{-(t-t^n)/\tau}-\tau\right)\left(a^LH[\tilde{u}]+a^R(1-H[\tilde{u}])\right)\tilde{u}f_0^+(\mathbf{x}_0,\mathbf{u}_0)\\
&+\left((t-t^n+\tau)\mathrm{e}^{-(t-t^n)/\tau}-\tau\right)(b\tilde{v}+c\tilde{w})\tilde{u}f_0^+(\mathbf{x}_0,\mathbf{u}_0)\\
&-\left((t-t^n+\tau)\mathrm{e}^{-(t-t^n)/\tau}-\tau\right)2\lambda(\mathbf{u}-\tilde{\mathbf{U}})\cdot\boldsymbol{\ell}f_0^+(\mathbf{x}_0,\mathbf{u}_0)\\
&+\left(t-t^n+\tau\left(\mathrm{e}^{-(t-t^n)/\tau}-1\right)\right)Af_0^+(\mathbf{x}_0,\mathbf{u}_0)\\
&+\mathrm{e}^{-(t-t^n)/\tau}\left(f_0^L(\mathbf{x}_0,\mathbf{u}_0)-(t-t^n)\mathbf{u}\cdot\frac{\partial f_0^L}{\partial\mathbf{x}}-(t-t^n)\boldsymbol{\ell}\cdot\frac{\partial f_0^L}{\partial\mathbf{u}}\right)H[\tilde{u}]\\
&+\mathrm{e}^{-(t-t^n)/\tau}\left(f_0^R(\mathbf{x}_0,\mathbf{u}_0)-(t-t^n)\mathbf{u}\cdot\frac{\partial f_0^R}{\partial\mathbf{x}}-(t-t^n)\boldsymbol{\ell}\cdot\frac{\partial f_0^R}{\partial\mathbf{u}}\right)(1-H[\tilde{u}]),
\end{aligned} \tag{3.22}$$

where $\tilde{u}=\mathbf{u}\cdot\mathbf{e}_1$, $\tilde{v}=\mathbf{u}\cdot\mathbf{e}_2$, $\tilde{w}=\mathbf{u}\cdot\mathbf{e}_3$. Based on the above time dependent distribution function at the cell interface, the UGKS flux can be calculated by Eq. (3.11), (3.12), and (3.13).

Denote the Jacobian matrix of the PHM system Eq. (2.9) as A_1 for x direction with eigenvectors $\boldsymbol{\ell}_1^p$ and $\mathbf{r}_1^p$, and A_2 for y direction with eigenvectors $\boldsymbol{\ell}_2^p$ and $\mathbf{r}_2^p$. The eigensystems of the Jacobian matrixes are given in Appendix B. The wave propagation method proposed by LeVeque [17, 37] is used to construct the numerical flux in Eq. (3.6), for

https://doi.org/10.4208/cicp.OA-2017-0102 Published online by Cambridge University Press

example

$$\left(\mathscr{F}_{\mathrm{Q}}^{x}\right)_{i-1/2,j}=\frac{1}{2}(A_1Q_{i,j}+A_1Q_{i-1,j})-\frac{1}{2}(A_1^+\Delta Q_{i-1/2}-A_1^-\Delta Q_{i-1/2}) \tag{3.23}$$

$$\begin{aligned}&+\frac{1}{2}\sum_p \mathrm{sign}(s^p_{i-1/2,j})\left(1-\frac{\Delta t}{\Delta x}|s^p_{i-1/2,j}|\right)\mathscr{L}^p_{1,i-1/2,j}\Phi(\theta^p_{1,i-/2,j})\\&-\frac{\Delta t}{2\Delta x}\mathbf{A}_\mathbf{1}^+\boldsymbol{\mathscr{A}}_2^-\Delta\mathbf{Q}_{i,j+1/2}-\frac{\Delta t}{2\Delta x}\mathbf{A}_\mathbf{1}^+\boldsymbol{\mathscr{A}}_2^+\Delta\mathbf{Q}_{i,j-1/2}\\&-\frac{\Delta t}{2\Delta x}\mathbf{A}_\mathbf{1}^-\boldsymbol{\mathscr{A}}_2^-\Delta\mathbf{Q}_{i+1,j+1/2}-\frac{\Delta t}{2\Delta x}\mathbf{A}_\mathbf{1}^-\boldsymbol{\mathscr{A}}_2^+\Delta\mathbf{Q}_{i+1,j-1/2},\end{aligned} \tag{3.24}$$

where

$$\mathscr{L}^p_{1,i-1/2,j}=\boldsymbol{\ell}^p_{1,i-1/2,j}\cdot(\mathbf{f}_{1,i,j}-\mathbf{f}_{1,i-1,j})\mathbf{r}^p_{1,i-1/2,j}. \tag{3.25}$$

$\Phi(\theta)$ is a limiter function [17] with

$$\theta^p_{1,i-1/2,j}\equiv\frac{\mathscr{L}^p_{1,I-1/2,j}\cdot\mathscr{L}^p_{1,i-1/2,j}}{\mathscr{L}^p_{1,i-1/2,j}\cdot\mathscr{L}^p_{1,i-1/2,j}},$$

with $I=i-1$ if $s^p_{i-1/2}>0$ and $I=i+1$ if $s^p_{i-1/2}<0$. The left and right going fluctuations are

$$\boldsymbol{\mathscr{A}}_2^\pm\Delta\mathbf{Q}_{i,j-1/2}=\mathbf{A}_\mathbf{1}^\pm\Delta\mathbf{Q}_{i,j-1/2}\mp\sum_p\mathrm{sign}(s^p_{i,j-1/2})\left(1-\frac{\Delta t}{\Delta x}|s^p_{i,j-1/2}|\right)\mathscr{L}^p_{1,i,j-1/2}\Phi(\theta^p_{1,i,j-1/2}). \tag{3.26}$$

An analogous expression can be derived for the Y directional flux.

3.3 Numerical treatment of particle acceleration and collision

In many cases, the electromagnetic acceleration is so large that the time step is restricted to be very small. In order to remove the constraint, we split the particle acceleration and collision process into two steps. First we shift the velocity distribution between cell centers, as shown in Fig. 5-i, which is based on the following considerations. The kinetic equation

$$\frac{\partial f}{\partial t}+\boldsymbol{\ell}\cdot\nabla_\mathbf{u}f=\frac{f^+-f}{\tau} \tag{3.27}$$

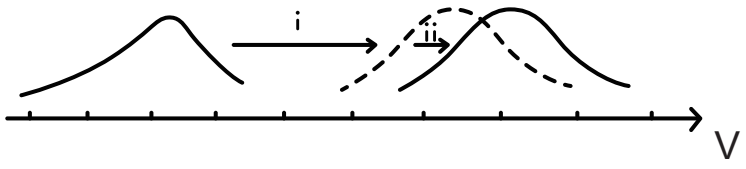


Figure 5: Two steps to update distribution function.

https://doi.org/10.4208/cicp.OA-2017-0102 Published online by Cambridge University Press

has exact solution

$$f(\mathbf{x},t,\mathbf{u})=f_0(\mathbf{x},\mathbf{u}-\boldsymbol{\ell}t)\mathrm{e}^{-t/\tau}+f^+(\mathbf{x},\mathbf{u}-\boldsymbol{\ell}t)(1-\mathrm{e}^{-t/\tau}). \tag{3.28}$$

Define $\mathbf{W}^*$ as

$$(\mathbf{W}_\alpha)_i^*=(\mathbf{W}_\alpha)_i^n-\frac{1}{|\Omega_{\mathbf{x}i}|}\sum_{s_i\in\partial\Omega_{\mathbf{x}i}}|s_i|\mathscr{F}_{\mathbf{W}_\alpha s_i}+\frac{\Delta t}{\tau_\alpha}\left((\bar{\mathbf{W}})_i^n-(\mathbf{W}_\alpha)_i^n\right), \tag{3.29}$$

based on which $\overline{\mathbf{W}}^*$ and f^{+*} can be obtained. Based the exact solution Eq. (3.28), the distribution functions are shifted as

$$f^{**}(u_k,v_l,w_m)=f^*(u_{k-su},v_{l-sv},w_{m-sw})\mathrm{e}^{-\Delta t_1/\tau}+f^{+*}(u_{k-su},v_{l-sv},w_{m-sw})(1-\mathrm{e}^{-\Delta t_1/\tau}), \tag{3.30}$$

where $su=\Delta t_1 l_u/\Delta u$, $sv=\Delta t_1 l_v/\Delta v$, $sw=\Delta t_1 l_w/\Delta w$, and

$$\Delta t_1=\min\left(\frac{\Delta u}{|l_u|}\left\lfloor\frac{|l_u|\Delta t}{\Delta u}\right\rfloor,\frac{\Delta v}{|l_v|}\left\lfloor\frac{|l_v|\Delta t}{\Delta v}\right\rfloor,\frac{\Delta w}{|l_w|}\left\lfloor\frac{|l_w|\Delta t}{\Delta w}\right\rfloor\right).$$

Then the distribution function is updated to the next time step as shown in Fig. 5-ii by

$$f^{n+1}=\left(f^{**}-\sum_{s_j\in\partial_{\Omega_{\mathbf{v}j}}}|s_j|\int_{t^n+\Delta t_1}^{t^{n+1}}\boldsymbol{\ell}\cdot\mathbf{n}f(\mathbf{x}_i,t,\mathbf{u}_{k+1/2})dt+\frac{\Delta t}{\tau^{n+1}}f^{+,n+1}\right)/\left(1+\frac{\Delta t}{\tau^{n+1}}\right), \tag{3.31}$$

where $f^{+,n+1}$ and τ^{n+1} are obtained from the updated conservative variables $\overline{\mathbf{W}}$. As $t^{n+1}-t^n-\Delta t_1$ is smaller than the relaxation time τ, the simplified upwind flux can be used in Eq. (3.31),

$$f(\mathbf{x}_i,t,\mathbf{u}_{k+1/2})=f(\mathbf{x}_i,t^n+\Delta t_1,\mathbf{u}_{k+1/2}). \tag{3.32}$$

In summary, the UGKS algorithm is shown as the flowchart in Fig. 6.

4 Limiting solutions of UGKS

4.1 Limits of UGKS flux in different regimes

Define the time averaged UGKS flux as

$$\tilde{F}_f=\frac{1}{\Delta t}\int_0^{\Delta t}\mathbf{u}f_{j+1/2}(t)dt. \tag{4.1}$$

In the limit of $\Delta t\ll\tau$, $\tilde{F}_f$ follows the particle transport and acceleration, which gives the Vlasov flux

$$\lim_{\Delta t/\tau\to 0}\tilde{F}_f=\mathbf{u}\left[f_{i+1/2}-\frac{1}{2}\Delta t\mathbf{u}\cdot\partial_{\mathbf{x}}f_{i+1/2}-\frac{1}{2}\Delta t\boldsymbol{\ell}\cdot\partial_{\mathbf{u}}f_{i+1/2}\right], \tag{4.2}$$

https://doi.org/10.4208/cicp.OA-2017-0102 Published online by Cambridge University Press

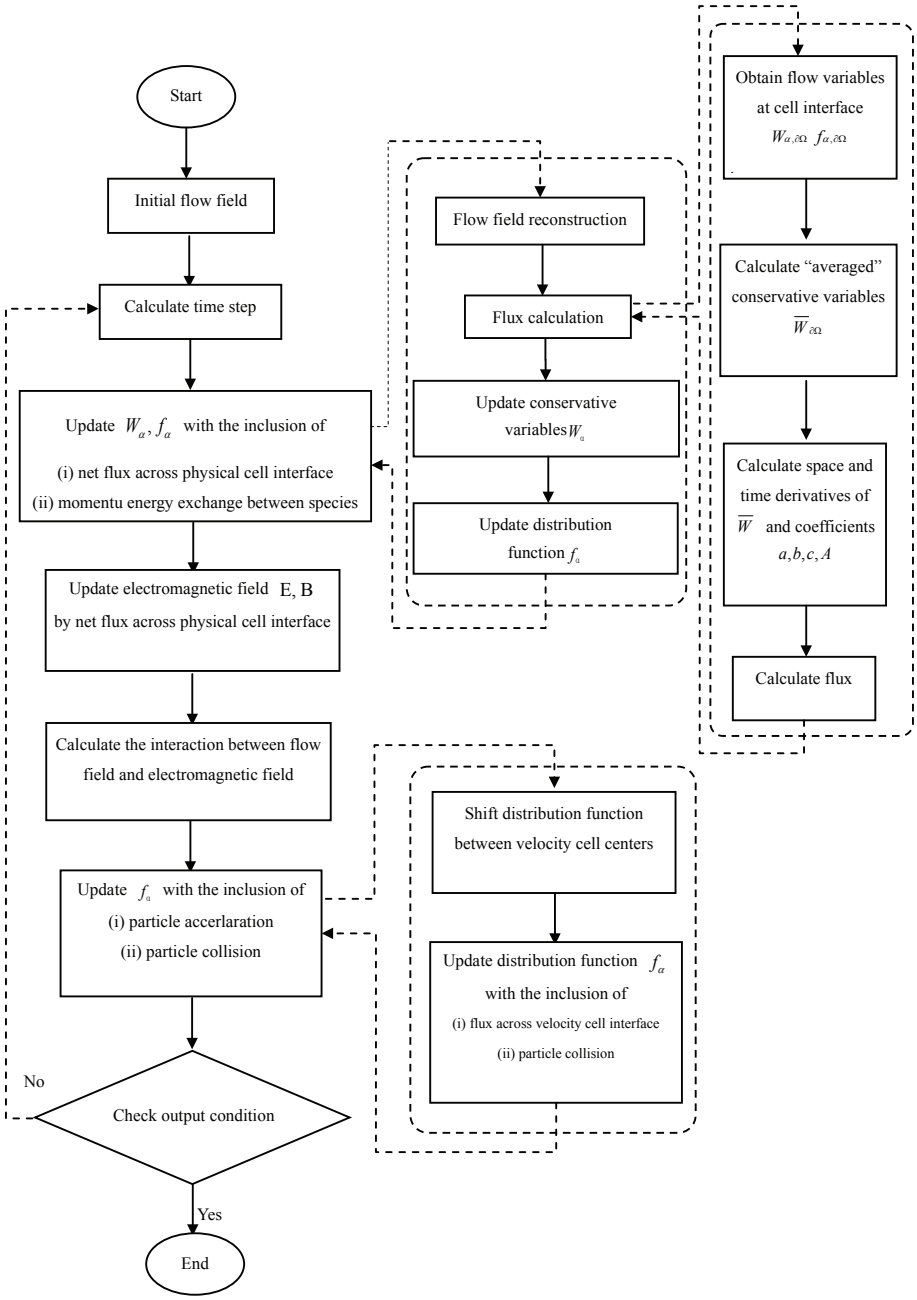


Figure 6: Flowchart of UGKS algorithm.

which is consistent with the collisionless Vlasov equation. In the limit of $\Delta t \gg \tau$, $\tilde{F}_f$ converge to the hydrodynamic flux, which gives

$$\lim_{\Delta t/\tau\to\infty} \tilde{F}_f = \mathbf{u}\left[g_{i+1/2} - \tau(\partial_t g_{i+1/2} + \mathbf{u}\cdot\partial_{\mathbf{x}} g_{i+1/2} + \boldsymbol{\ell}\cdot\partial_{\mathbf{u}} g_{i+1/2}) + \frac{1}{2}\Delta t\partial_t g_{i+1/2})\right], \tag{4.3}$$

https://doi.org/10.4208/cicp.OA-2017-0102 Published online by Cambridge University Press

from which the hydrodynamic two-fluid system can be recovered, as well as the MHD equations. The flow dynamics depends on the ratio of local time step Δt to the relaxation parameter τ. In other words, the UGKS models the plasma evolution on the scales of the cell size and time step.

4.2 Limits of the source terms for different kinds of MHD equations

Define $\mathbf{U}_\alpha^*$, and $\mathbf{E}^*$ as

$$\begin{aligned}
&\left(\rho_\alpha^{n+1}\mathbf{U}_\alpha^*\right)_i = (\rho_\alpha \mathbf{U}_\alpha)_i^n - \frac{1}{|\Omega_{\mathbf{x}i}|}\sum_{s_i\in\partial\Omega_{\mathbf{x}i}} |s_i|\mathscr{F}_{\rho_\alpha U_\alpha s_i} + \frac{\Delta t}{\tau_\alpha}\left((\rho_\alpha \overline{\mathbf{U}}_\alpha)_i^n - (\rho_\alpha \mathbf{U}_\alpha)_i^n\right),\\
&\mathbf{E}_i^* = \mathbf{E}_i^n + \frac{\Delta t}{|\Omega_{\mathbf{x}i}|}\sum_{s_i\in\partial\Omega_{\mathbf{x}i}} |s_i|\mathscr{F}_{\mathbf{E}s_i}.
\end{aligned} \tag{4.4}$$

The update equations of momentum and electric field in UGKS, Eqs. (3.4), (3.7), and (3.9) are

$$\begin{cases}
\rho_i^{n+1}\mathbf{U}_i^{n+1} - \rho_i^{n+1}\mathbf{U}_i^* = \dfrac{\Delta t}{r_{L_i}} n_i^{n+1}(\mathbf{E}^{n+1} + \mathbf{U}_i^{n+1}\times\mathbf{B}^{n+1}),\\
\rho_e^{n+1}\mathbf{U}_e^{n+1} - \rho_e^{n+1}\mathbf{U}_e^* = -\dfrac{\Delta t}{r_{L_i}} n_e^{n+1}(\mathbf{E}^{n+1} + \mathbf{U}_e^{n+1}\times\mathbf{B}^{n+1}),\\
\mathbf{E}^{n+1} - \mathbf{E}^* = -\dfrac{\Delta t}{\lambda_D^2 r_{L_i}}\left(\mathbf{j}_i^{n+1} + \mathbf{j}_e^{n+1}\right),\\
\phi^{n+1} - \phi^* = \dfrac{\Delta t\chi}{\lambda_D^2 r_{L_i}}(n_i^{n+1} - n_e^{n+1}),
\end{cases} \tag{4.5}$$

which can be rearranged as the following linear system

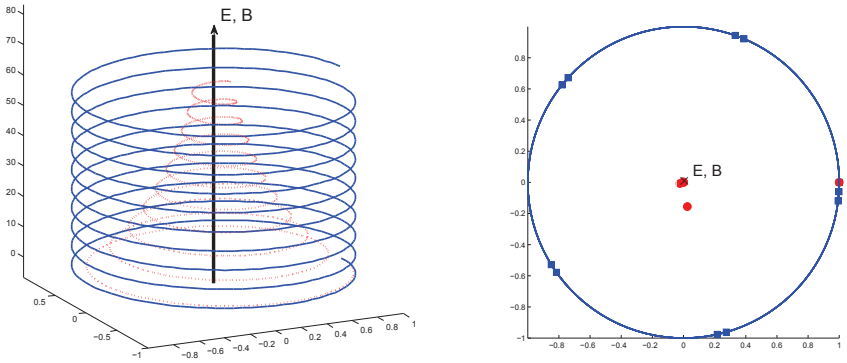
$$\begin{cases}
\displaystyle\sum_\alpha m_\alpha n_\alpha^{n+1}\mathbf{U}_\alpha^{n+1} - r_{L_i}^{-1}(n_i^{n+1} - n_e^{n+1})\Delta t\mathbf{E}^{n+1} + \lambda_D^2\mathbf{E}^{n+1}\times\mathbf{B}^{n+1}\\
\qquad = \lambda_D^2\mathbf{E}^*\times\mathbf{B}^{n+1} + \displaystyle\sum_\alpha m_\alpha n_\alpha^{n+1}\mathbf{U}_\alpha^*, & (4.6)\\
\Delta t(n_e^{n+1}\mathbf{E}^{n+1} + n_e^{n+1}\mathbf{U}_e\times\mathbf{B}^{n+1}) + r_{L_i} m_e n_e^{n+1}\mathbf{U}_e^{n+1} = r_{L_i} m_e n_e^{n+1}\mathbf{U}_e^*, & (4.7)\\
\Delta t(n_i^{n+1}\mathbf{U}_i^{n+1} - n_e^{n+1}\mathbf{U}_e^{n+1}) + \lambda_D^2 r_{L_i}\mathbf{E}^{n+1} = \lambda_D^2 r_{L_i}\mathbf{E}^*, & (4.8)\\
\lambda_D^2 r_{L_i}\phi^{n+1} = \Delta t\chi(n_i^{n+1} - n_e^{n+1}) + \lambda_D^2 r_{L_i}\phi^*. & (4.9)
\end{cases}$$

The implicit source term treatment endows the UGKS with the following two properties.

First, the time step is not restricted by the cyclotron period. As shown in Fig. 7 that the linear system Eq. (4.5) are contract projection with respect to the helical motion of the charged particles. The motion of particles will be confined to the magnetic field lines as time step getting large, which ensures the stability of the scheme.

Second, the asymptotic limits of the BGK-Maxwell system are preserved. As $r_{L_i}, \lambda_D \to 0$, Eq. (4.8) preserves the synchronous motion of electron and ion, and the quasi-neutrality

https://doi.org/10.4208/cicp.OA-2017-0102 Published online by Cambridge University Press



a b

Figure 7: Helical trajectory calculated by semi-implicit scheme (solid line and square symbols) and by fully implicit scheme (dotted line and circular symbols). Time step is set to be (a) $\Delta t=0.2\omega_c^{-1}$, and (b) $\Delta t=2\omega_c^{-1}$.

of plasma

$$(\mathbf{j}_i+\mathbf{j}_e)^{n+1}=-r_{L_i}\lambda_D^2\frac{\mathbf{E}^{n+1}-\mathbf{E}^*}{\Delta t}$$
$$\xrightarrow{r_{L_i},\lambda_D\to 0} \quad n_i^{n+1}\mathbf{U}_i^{n+1}=n_e^{n+1}\mathbf{U}_e^{n+1},\ \nabla\cdot\mathbf{j}=0, \tag{4.10}$$

from which one can derive $(n_i-n_e)\sim\mathcal{O}(\lambda_D^2 r_{L_i})$ provided that the system is quasi-neutral initially. As $r_{L_i}\to 0$, Eq. (4.7) converges to the ideal Ohm's law

$$(n_e\mathbf{E}+n_e\mathbf{U}_e\times\mathbf{B})^{n+1}=-\frac{r_{L_i}}{\Delta t}(\rho_e^{n+1}\mathbf{U}_e^{n+1}-\rho_e^{n+1}\mathbf{U}_e^*)$$
$$\xrightarrow{r_{L_i}\to 0} \quad \mathbf{E}^{n+1}+\mathbf{U}^{n+1}\times\mathbf{B}^{n+1}=0. \tag{4.11}$$

As $r_{L_i}\to 0$ and $\lambda_D\sim c^{-1}$, Eq. (4.6) gives $n_e^{n+1}=n_i^{n+1}$ and the MHD momentum equation

$$\sum_\alpha\frac{m_\alpha\mathbf{U}_\alpha^{n+1}-m_\alpha\mathbf{U}_\alpha^*}{\Delta t}=\frac{\mathbf{E}^{n+1}}{r_{L_i}}(n_i-n_e)^{n+1}-\lambda_D^2\frac{\mathbf{E}^{n+1}-\mathbf{E}^*}{\Delta t}\times\mathbf{B}^{n+1}$$
$$\xrightarrow[\lambda_D\sim c^{-1}]{r_{L_i}\to 0} \quad \sum_\alpha\frac{m_\alpha\mathbf{U}_\alpha^{n+1}-m_\alpha\mathbf{U}_\alpha^*}{\Delta t}\approx(\nabla\times\mathbf{B}^n)\times\mathbf{B}^{n+1}. \tag{4.12}$$

In the limit of $r_{L_i}\to 0$, the linear system (4.6)-(4.9) becomes

$$\begin{cases}\sum_\alpha m_\alpha n_\alpha^{n+1}\mathbf{U}_\alpha^{n+1}+\lambda_D^2\mathbf{E}^{n+1}\times\mathbf{B}^{n+1}\\ \qquad=\lambda_D^2\mathbf{E}^*\times\mathbf{B}^{n+1}+\sum_\alpha m_\alpha n_\alpha^{n+1}\mathbf{U}_\alpha^*,\\ \mathbf{E}^{n+1}+\mathbf{U}_e\times\mathbf{B}^{n+1}=0,\\ \mathbf{U}_i^{n+1}=\mathbf{U}_e^{n+1},\\ \phi^{n+1}=\phi^n.\end{cases} \tag{4.13}$$

https://doi.org/10.4208/cicp.OA-2017-0102 Published online by Cambridge University Press

In this quasi-neutral regime, the electric field is automatically calculated from the Ohm's law. Eq. (4.11) indicates that UGKS provides a smooth transition from the Ampère's Law to the ideal Ohm's law with a decreasing of the Larmor radius r_{L_i}, which can remove the speed of light constraint on time step in the continuum MHD regime. For large r_{L_i}, the time step constraint of UGKS is

$$\Delta t = \frac{\text{CFL}\Delta x}{\max(U+4c_s,c)} = \text{CFL}\frac{\Delta x}{c}. \tag{4.14}$$

The CFL number increases as r_{L_i} decreases. For example, in the Brio-Wu shock test case in the next section, CFL$=0.3$ for $r_{L_i}<1$, CFL$=0.4$ for $r_{L_i}=10^{-1}$, CFL$=0.5$ for $r_{L_i}=10^{-2}$, CFL$=1.2$ for $r_{L_i}=10^{-3}$. When r_{L_i} is set to be zero for ideal MHD solutions, the time step will not be limited by the speed of light, and is determined by

$$\Delta t = \text{CFL}\frac{\Delta x}{U+\max(c_m,4c_s)}, \tag{4.15}$$

where c_s is the sound speed and c_m is the fast magneto-sound speed.

5 Numerical experiments

In this section, the UGKS is tested for cases from the collisionless regime to the MHD one. In the collisionless Vlasov regime, we consider the classical test cases of Landau damping and two stream instability. The relaxation parameter τ in Vlasov limit is set to be $\tau=10^3$ (in program $\exp(-\Delta t/\tau)$ is assigned to 1 in order to avoid machine error). For these test cases, we view ions as a fixed background and consider the motion of electrons. The reason for the setting is that there is corresponding reference solutions under such a condition. Because no magnetic field is involved, and the Maxwell equations degenerate to the Poisson equation, so the FFT-based Poisson solver can be used to calculate the electric field. In MHD regime, we first calculate the one dimensional Brio-Wu shock tube test case. With the reduction of normalized Larmor radius, the solution goes from the Euler solution to Hall-MHD solution, and finally converges to the ideal-MHD solution. For two dimensional test cases, we first consider the Orszag-Tang MHD turbulence problem which tests the performance of UGKS in capturing MHD solutions. After testing UGKS in both limiting regimes, the scheme is used to study the GEM magnetic reconnection problem, which happens on the Debye length scale.

In order to reduce computational cost, the reduced distribution functions are used in our numerical calculation. For the x-dimensional Brio-Wu shock tube problem which is homogeneous in the y,z-dimensional physical space, the reduced distributions are defined as

$$\begin{aligned} h_{\alpha,0}(u) &= \int_{-\infty}^{\infty}\int_{-\infty}^{\infty} f_\alpha dvdw, \quad h_{\alpha,1}(u) = \int_{-\infty}^{\infty}\int_{-\infty}^{\infty} v f_\alpha dvdw, \\ h_{\alpha,2}(u) &= \int_{-\infty}^{\infty}\int_{-\infty}^{\infty} w f_\alpha dvdw, \quad h_{\alpha,3}(u) = \int_{-\infty}^{\infty}\int_{-\infty}^{\infty} (v^2+w^2) f_\alpha dvdw. \end{aligned} \tag{5.1}$$

https://doi.org/10.4208/cicp.OA-2017-0102 Published online by Cambridge University Press

Similarly, the reduced post-collision distributions are defined as

$$\begin{aligned}
H_{\alpha,0} &= \int f_\alpha^+ dw = \rho_\alpha \sqrt{\frac{\bar{\lambda}_\alpha}{\pi}} \exp\left(-\bar{\lambda}_\alpha((u-\bar{U}_\alpha)^2)\right), \\
H_{\alpha,1} &= \int v f_\alpha^+ dw = \rho_\alpha V_\alpha \sqrt{\frac{\bar{\lambda}_\alpha}{\pi}} \exp\left(-\bar{\lambda}_\alpha((u-\bar{U}_\alpha)^2)\right), \\
H_{\alpha,2} &= \int w f_\alpha^+ dw = \rho_\alpha W_\alpha \sqrt{\frac{\bar{\lambda}_\alpha}{\pi}} \exp\left(-\bar{\lambda}_\alpha((u-\bar{U}_\alpha)^2)\right), \\
H_{\alpha,3} &= \int (v^2+w^2) f_\alpha^+ dw = \rho_\alpha \left(V_\alpha^2 + W_\alpha^2 + \frac{1}{\bar{\lambda}_\alpha}\right) \sqrt{\frac{\bar{\lambda}_\alpha}{\pi}} \exp\left(-\bar{\lambda}_\alpha((u-\bar{U}_\alpha)^2)\right).
\end{aligned} \tag{5.2}$$

And the reduced BGK equation can be derived as

$$\begin{aligned}
&\frac{\partial h_0}{\partial t} + u\frac{\partial h_0}{\partial x} + l_1 \frac{\partial h_0}{\partial u} = \frac{H_0 - h_0}{\tau}, \\
&\frac{\partial h_1}{\partial t} + u\frac{\partial h_1}{\partial x} + l_1 \frac{\partial h_1}{\partial u} = \frac{H_1 - h_1}{\tau} + l_2 h_0, \\
&\frac{\partial h_2}{\partial t} + u\frac{\partial h_2}{\partial x} + l_1 \frac{\partial h_2}{\partial u} = \frac{H_2 - h_2}{\tau} + l_3 h_0, \\
&\frac{\partial h_3}{\partial t} + u\frac{\partial h_3}{\partial x} + l_1 \frac{\partial h_3}{\partial u} = \frac{H_2 - h_2}{\tau} + 2l_2 h_1 + 2l_3 h_2.
\end{aligned} \tag{5.3}$$

Similarly for the two dimensional Orszag-Tang Vortex and magnetic reconnection problem, the reduced distributions are defined as

$$h_{\alpha,0}(u,v) = \int f dw, \quad h_{\alpha,1}(u,v) = \int w f dw, \quad h_{\alpha,2}(u,v) = \int w^2 f dw. \tag{5.4}$$

And the corresponding reduced BGK equations can be derived. Therefore, in the following numerical test cases, the numerical velocity space is one dimensional for Brio-Wu shock, multiple scale shock tube problem, and the numerical velocity space is two dimensional for Orszag-Tang Vortex, magnetic reconnection problem. The numerical fluxes for the two dimensional reduced distributions are given in Appendix C.

5.1 Linear Landau damping

A Vlasov-Poisson (VP) system is perturbed by a weak signal. The linear theory of Landau damping can be applied to predict the linear decay of electric energy with time [2]. The initial condition of linear Landau damping for the Vlasov Poisson system is

$$f_0(x,u) = \frac{1}{\sqrt{2\pi}}(1+\alpha\cos(kx))\mathrm{e}^{-\frac{u^2}{2}}, \tag{5.5}$$

with $\alpha = 0.01$. The length of the domain in the x direction is $L = 2\pi/k$. The background ion distribution function is fixed, uniformly chosen so that the total net charge density for

https://doi.org/10.4208/cicp.OA-2017-0102 Published online by Cambridge University Press

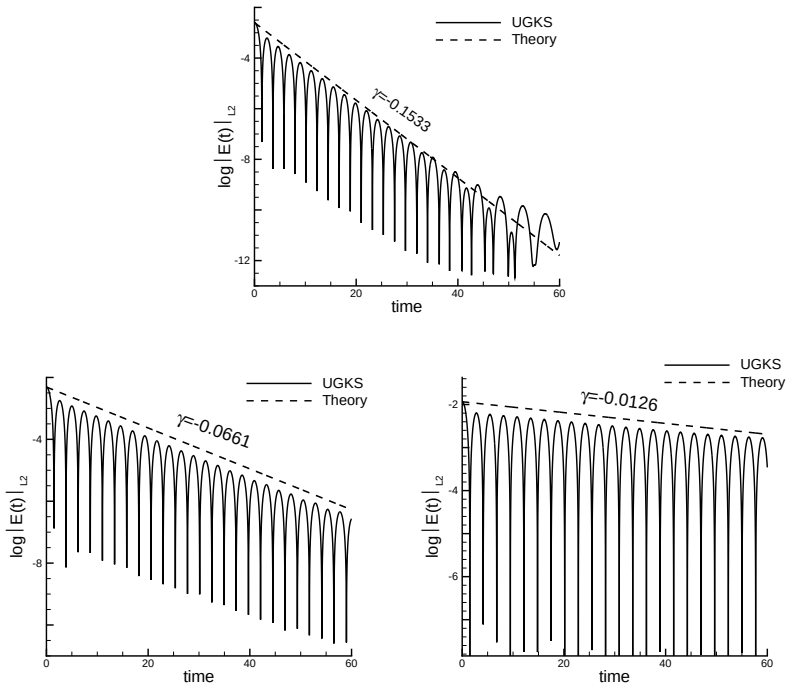


Figure 8: Weak Landau damping. Time evolution of electric field in L^2 norm. $k=0.5$ (upper), $k=0.4$ (lower left) and $k=0.3$ (lower right).

the system is zero. When perturbation parameter $\alpha=0.01$ is small enough, the Vlasov-Poisson system can be approximated by linearization around the Maxwellian equilibrium. The analytical damping rate of electric field can be derived accordingly. We test our scheme with different wave numbers and compare the numerical damping rates with theoretical values. The phase space is discretized with $N_x\times N_u=128\times128$ cells with $u_{\max}=5U_0$. We plot the evolution of electric field in L^2 norm in Fig. 8 for $k=0.5$, $k=0.4$, and $k=0.3$. The correct decay rates of the electric field are observed and are matched with theoretical values. In addition, the frequencies of oscillating solutions consist with the theoretical values of $\omega=1.41$, $\omega=1.29$, $\omega=1.16$. The profile of velocity distribution $f(x=0,u,t)$ is plotted in Fig. 9, which shows that the particles with low velocity absorb energy from the electric wave.

5.2 Nonlinear Landau damping

When the VP system is perturbed by a large amplitude, the nonlinear effect will appear [2]. For nonlinear landau damping, the initial condition is similar to the linear case while the parameters are set as $\alpha=0.5$ and $k=0.5$. The mesh size is set to be $N_x\times N_u=256\times256$. Fig. 10 shows the L^2 norms of electric field computed by UGKS. The linear decay rate

https://doi.org/10.4208/cicp.OA-2017-0102 Published online by Cambridge University Press

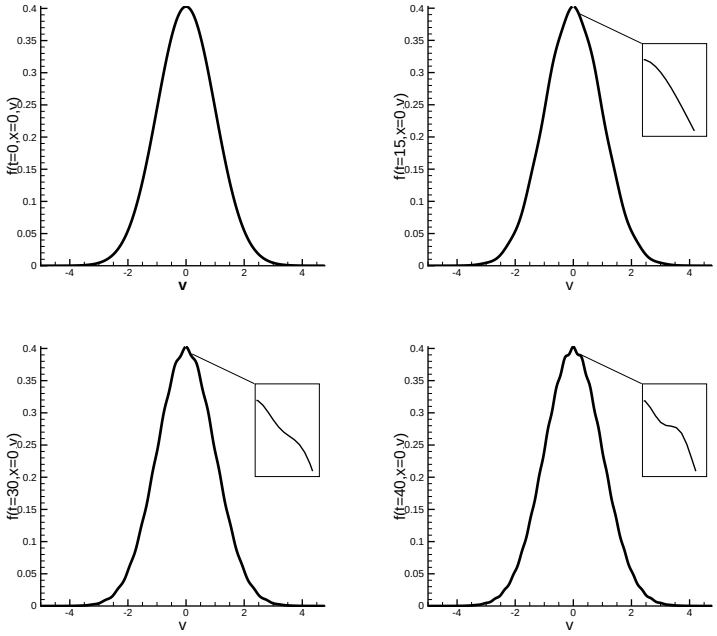


Figure 9: Time development of the distribution function at $x=0$.

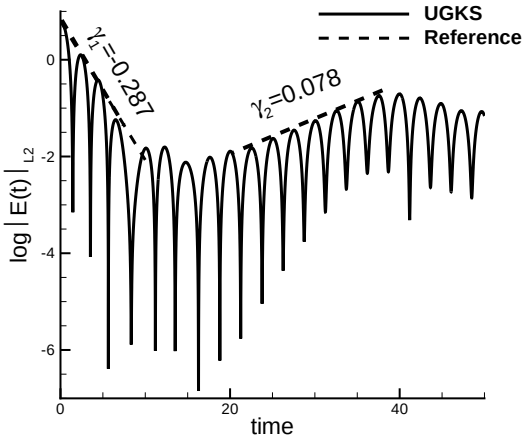


Figure 10: Strong Landau damping. Time evolution of electric field in L^2 norm.

of electric energy is approximately equal to $\gamma_1=-0.287$, which is identical to the value obtained by Heath *et al.*. The growth rate provided by UGKS is approximately $\gamma_2=0.078$, which is between the value of 0.0815 computed by Rossmanith and Seal and 0.0746 by Heath *et al.*. The contours of velocity distribution at different times are shown in Fig. 11.

https://doi.org/10.4208/cicp.OA-2017-0102 Published online by Cambridge University Press

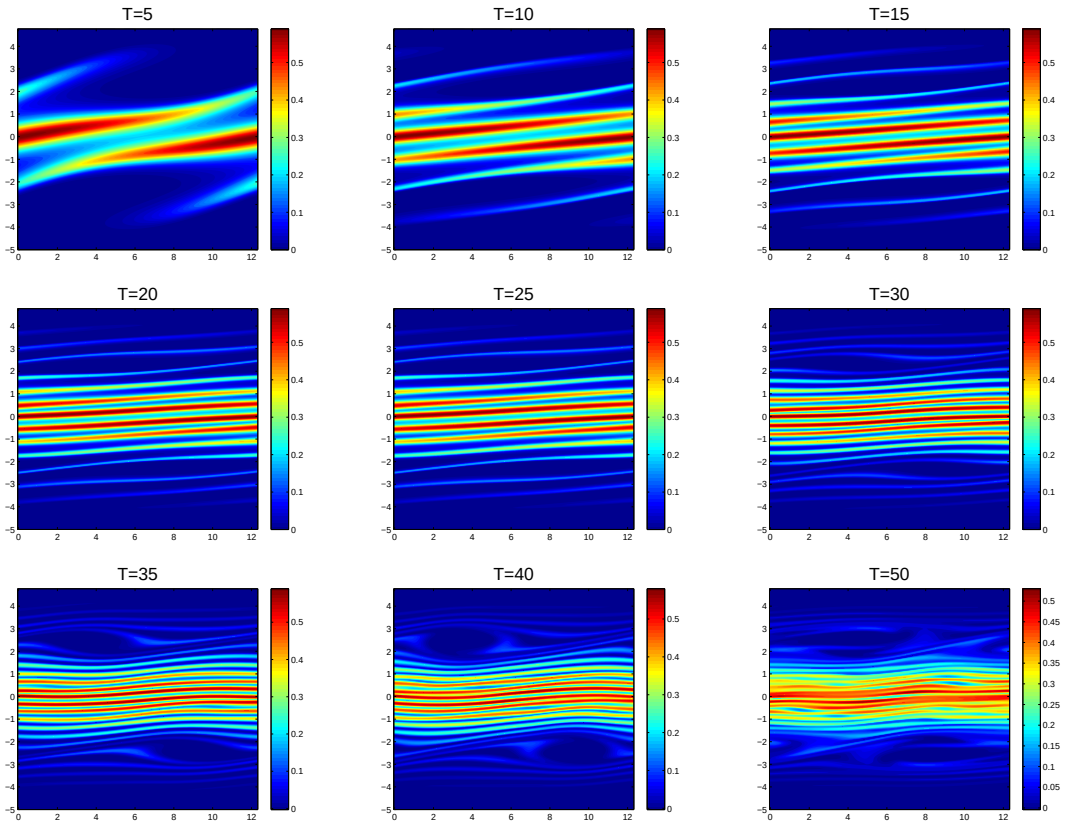


Figure 11: Strong Landau damping. Velocity distribution contours. $N_x \times N_u = 256 \times 256$.

The profile of velocity distribution at $x = 0$ is plotted in Fig. 12, from which the nonlinear effect is clearly observed.

5.3 Linear two stream instability

Consider linear two stream instability problem with initial distribution function:

$$f(x,u,t=0) = \frac{2}{7\sqrt{2\pi}}(1+5v^2)(1+\alpha((\cos(2kx)+\cos(3kx))/1.2+\cos(kx)))e^{-\frac{u^2}{2}}, \quad (5.6)$$

where $\alpha = 0.001$ and $k = 0.2$. The length of the domain in the x direction is $L = \frac{2\pi}{k}$. The background ion distribution function is fixed, uniformly to balance the charge density of electron. After an initial transition, a linear growth rate of electric field can be found, and the value can be theoretically calculated [2]. In Fig. 13, we plot the evolution of electric field in L^2 norm. The growth rate predicted by UGKS is the same as the theoretical one. The velocity distribution contours at time $t = 70$ with mesh sizes $N_x \times N_u = 256 \times 256$ and $N_x \times N_u = 512 \times 512$ are presented in Fig. 14.

https://doi.org/10.4208/cicp.OA-2017-0102 Published online by Cambridge University Press

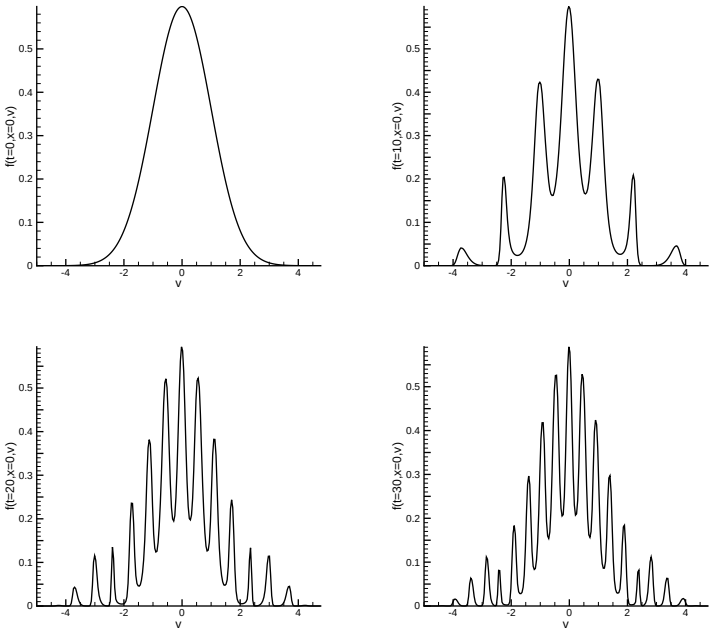


Figure 12: Strong Landau damping. Time development of the distribution function at $x=0$.

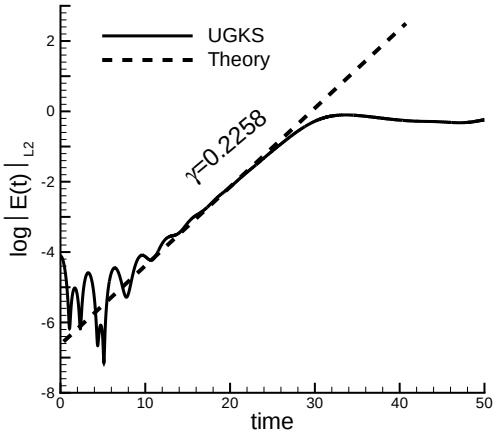


Figure 13: Two stream instability. Time evolution of electric field in L^2 norm. $\alpha=0.001$, $u_{th}=1$ and $k=0.2$.

5.4 Nonlinear two stream instability

For the nonlinear case of two stream instability, we use a symmetric initial condition

$$f(x,u,t=0)=\frac{1}{2v_{th}\sqrt{2\pi}}\left[\exp\left(-\frac{(u-U)^2}{2u_t^2}\right)+\exp\left(-\frac{(u+U)^2}{2u_t^2}\right)\right](1+\alpha\cos(kx)), \quad (5.7)$$

https://doi.org/10.4208/cicp.OA-2017-0102 Published online by Cambridge University Press

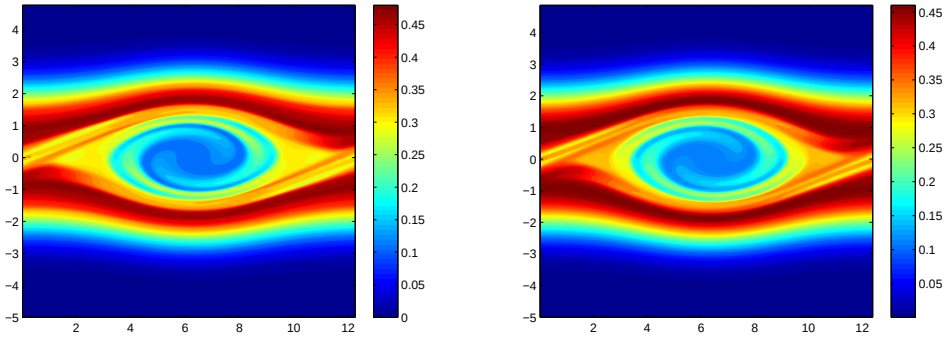


Figure 14: Two stream instability (weak). Velocity distribution contours at $t=70$. $N_x\times N_u=256\times256$ (left); $N_x\times N_u=512\times512$ (right).

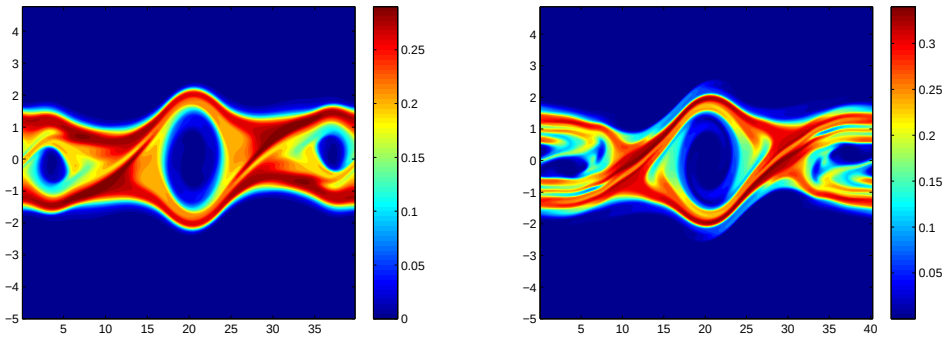


Figure 15: Two stream instability (nonlinear). Velocity distribution contours at $t=70$. $N_x\times N_u=256\times256$ (left); $N_x\times N_u=512\times512$ (right)

with $\alpha=0.05$, $U=0.99$, $u_t=0.3$, and $k=\frac{2}{13}$. In Fig. 15, we show the numerical results of the contours of distribution function at $t=70$. The computations show that the detailed structures of f can only be captured with very fine mesh $N_x\times N_u=512\times512$ for a second order scheme.

5.5 Brio-Wu shock tube

The Brio-Wu shock tube is a standard test case for ideal MHD solvers in continuum regime [13, 17]. The same initial condition as the Brio-Wu one is shown in Fig. 16. The initial correct potential ϕ and ψ for electromagnetic field are set to be zero. The ion to electron mass ratio is set to be 1836, and the ionic charge state is set to be unity. The Knudsen number of the following test case is set to be 10^{-5}, and ν_{ie} is defined the same as the one in the original AAP model [33]. The normalized Debye length is 0.01, and the normalized speed of light is 100. The ion Larmor radius takes different values normal-

https://doi.org/10.4208/cicp.OA-2017-0102 Published online by Cambridge University Press

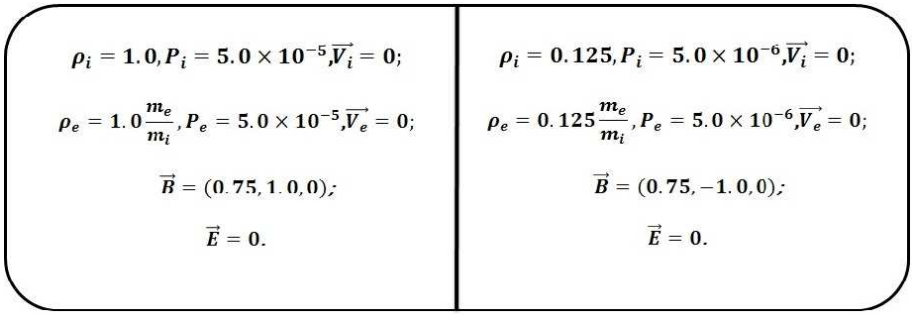


Figure 16: Initial condition for Brio-Wu shock tube problems.

ized by the length of the domain, i.e. $r_{L_i} = 100, 0.01, 0.003$. The grid points in physical space are 1000. The velocity space is $[-5,5]$ for ion and $[-5\sqrt{1836}, 5\sqrt{1836}]$ for electron with 32 grid points.

In this test case, different time steps for electron and ion are used to reduce the computational cost. Specifically, based on the CFL number, the time step Δt_i for ions is chosen to be five times of the time step Δt_e for electrons. During one Δt_e the ions are supposed to be fixed, after evolving the electrons five times with Δt_e each, we update ions for one Δt_i and couple them with electrons through electromagnetic field.

The averaged density and velocity are calculated by

$$\rho = \frac{\rho_i m_i + \rho_e m_e}{m_i + m_e}, \quad \mathbf{U} = \frac{\mathbf{U}_i m_i + \mathbf{U}_e m_e}{m_i + m_e}.$$

The results of the density, velocity, and magnetic field profiles, which are compared with the gas dynamic results, and MHD results are shown in Fig. 17. It can be observed that the solutions behave like Euler solutions at large normalized Larmor radius. When normalized Larmor radius gets small, the behavior of plasma fluid follows the Hall-MHD and towards to ideal MHD solutions.

5.6 Multiple scale shock tube problem

In this calculation, we study how the solution is developed from the initial condition to the final MHD one. Multi-scale solutions can be observed at different output times. The ion to electron mass ratio is set to be 25 and ν_{ie} is set to be zero. The characteristic length is fixed to be 1000 ion Larmor radius. The upstream Debye length is $0.01 r_{L_i}$. The velocity space is $[-3,3]$ for ion and $[-15,15]$ for electron with 16 grid points. Based on different output times, the cell size is initially fixed with different value. The ion number density at times $t = 10^{-5}, 10^{-4}, 10^{-3}, 10^{-2}, 10^{-1}$ by UGKS are shown in Fig. 18, which are compared with the Vlasov solutions and hydrodynamic two-fluid solutions. The relative Knudsen number Kn for each output solution, which is defined as the ratio between the mean free path ℓ and the plotted domain length L is $\mathrm{Kn} = 10^{-1}, 10^{-2}, 10^{-3}, 10^{-4}, 10^{-5}$

https://doi.org/10.4208/cicp.OA-2017-0102 Published online by Cambridge University Press

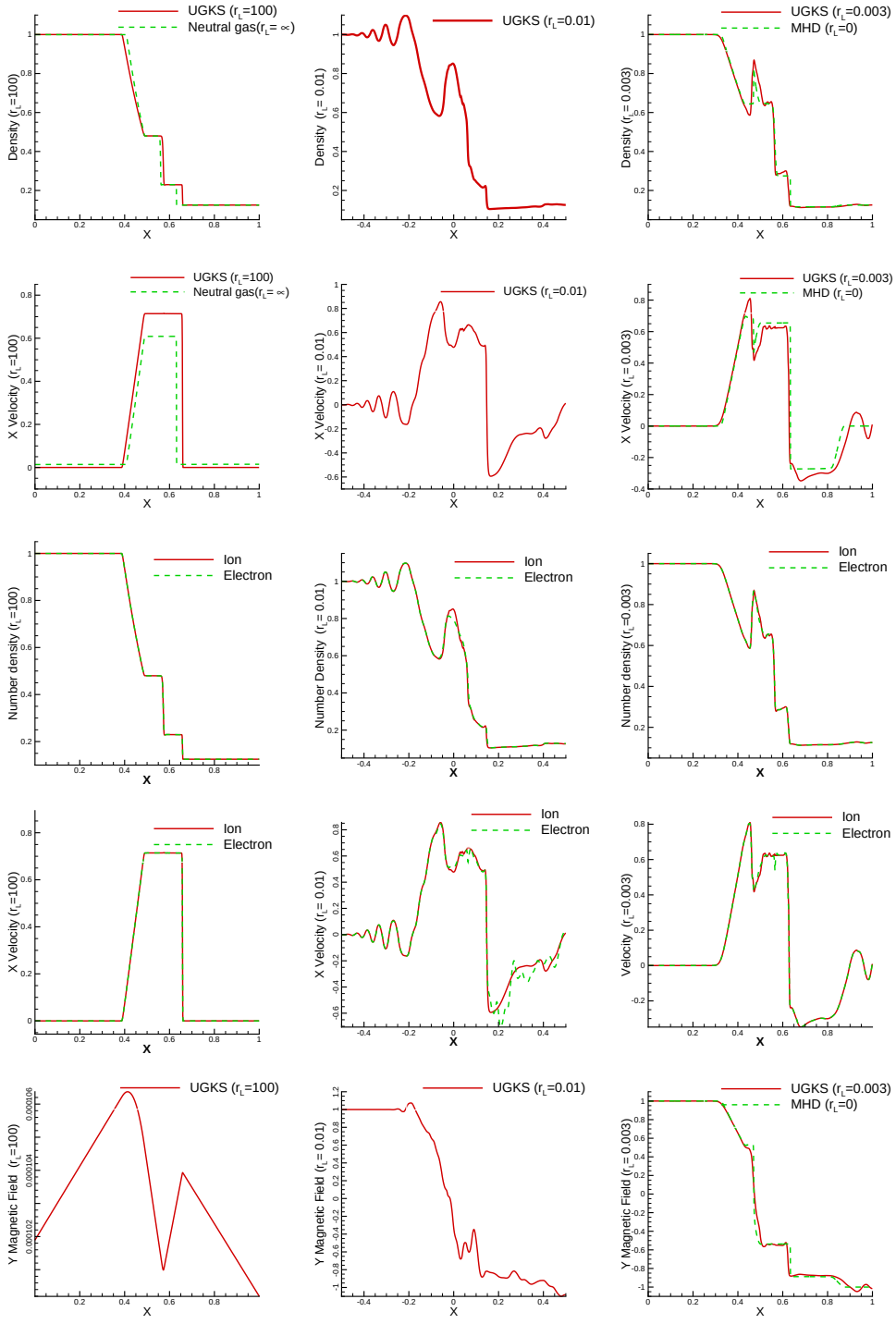


Figure 17: Results of the averaged density, averaged velocity, ion-electron density, ion-electron velocity, and magnetic field profiles from top to bottom, at $r_{L_i} = 100, 0.01, 0.003$ from left to right.

https://doi.org/10.4208/cicp.OA-2017-0102 Published online by Cambridge University Press

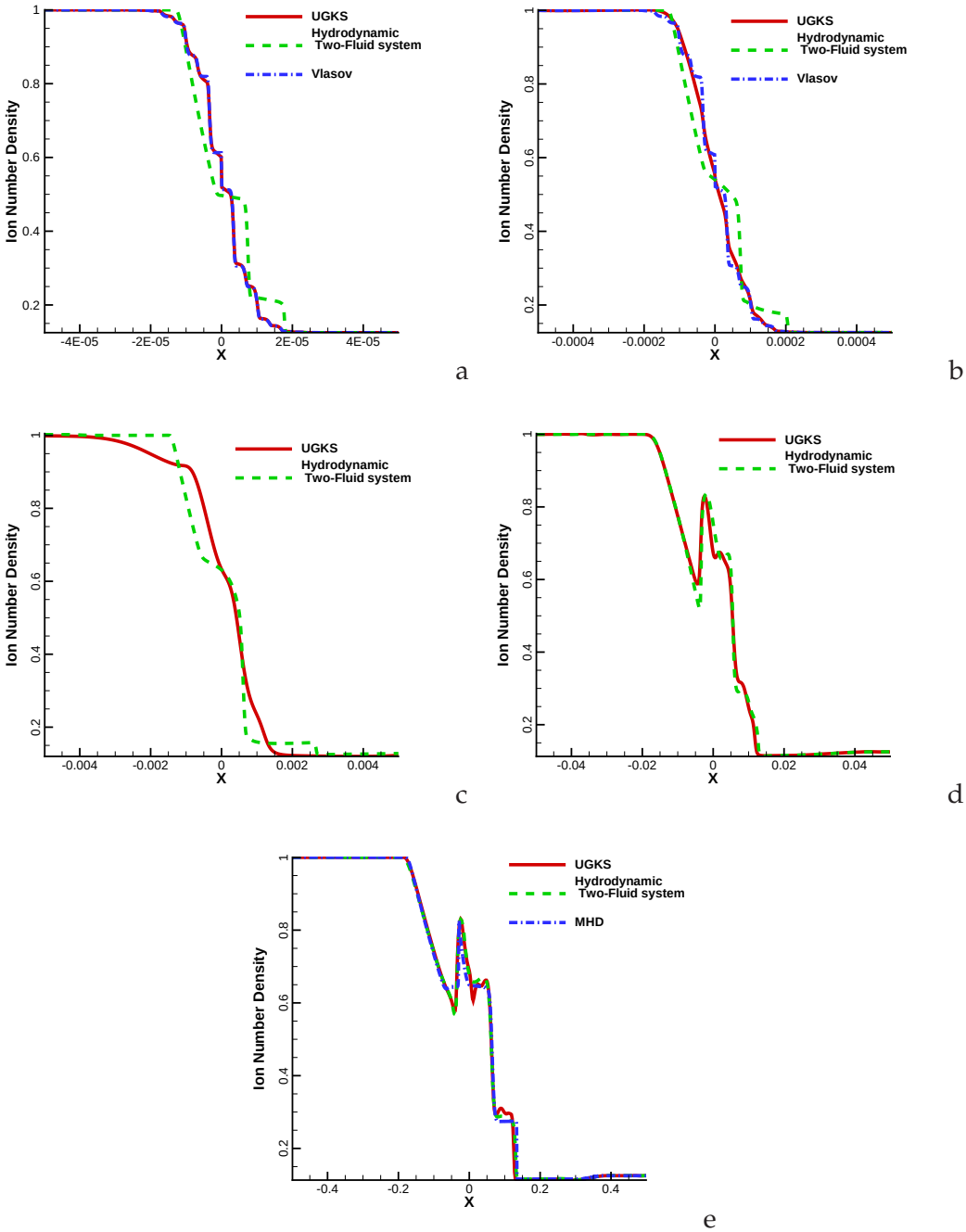


Figure 18: Solutions of the Brio-Wu shock tube at output times $t=10^{-5}$ (a), 10^{-4} (b), 10^{-3} (c), 10^{-2} (d), 10^{-1} (e). The UGKS solutions are compared with the two fluid system solutions, Vlasov solutions (for $t=10^{-5}$,10^{-4}) and MHD solution (for $t=10^{-1}$).

https://doi.org/10.4208/cicp.OA-2017-0102 Published online by Cambridge University Press

for solutions (a)-(e) in Fig. 18. For the solution at $t=10^{-5}$, the cell size is 2.0×10^{-7}, which is much less than the ion Larmor radius $\Delta x=2\times10^{-4}r_{L_i}$, and the time step is $\Delta t=3\times10^{-3}\tau_i=2\times10^{-3}\omega_{pi}^{-1}$. At this output time, the UGKS solution goes to Vlasov one due to this collisionless limit, which is different from the hydrodynamic two-fluid solutions. The cell sizes used for solutions with output times $t=10^{-4},10^{-3},10^{-2}$ are $\Delta x=2.0\times10^{-6},2.0\times10^{-5},2.0\times10^{-4}$ respectively. In the transition regime, in comparison with the solutions from the Vlasov and hydrodynamic two-fluid equations, the solution of UGKS should be physically reliable. A large cell size $\Delta x=2\times10^{-3}$ is used for the solution with the output time $t=0.1$, and this cell size is two times as large as the ion Larmor radius, and the time step for this case is $\Delta t=30\tau_i=25\omega_{pi}^{-1}$. It is shown that at the output time $t=0.1$, both the UGKS and two fluid system solutions converge to the MHD solution in this hydrodynamic regime. The computational time for UGKS to get solution at $t=0.1$ is 126 seconds on a 3.40GHz 4-core CPU machine.

5.7 Orszag-Tang vortex

This problem was introduced by Orszag and Tang as a simple model to study MHD turbulence [38,39]. The mass ratio is set as $m_i/m_e=25$, the Knudsen number is 10^{-5} and the Larmor radius is set to be zero for ideal MHD solutions first. The initial data for the current study is

$$n_i=n_e=\gamma^2,\quad P_i=P_e=\gamma,\quad B_y=\sin(2x),$$
$$u_{i,x}=u_{e,x}=-\sin(y),\quad u_{i,y}=u_{e,y}=\sin(x),$$

where $\gamma=5/3$. The electromagnetic correction potentials are set $\phi=\psi=0$ initially. The interspecies collision factor ν_{ie} is set to be zero. The computation domain is $[0,2\pi]\times[0,2\pi]$ with a uniform mesh of 200×200 cells. The velocity space for ion is $[-3,3]\times[-3,3]$ and for electron is $[-5\sqrt{5},5\sqrt{5}]\times[-5\sqrt{5},5\sqrt{5}]$ with 32×32 velocity grids. Periodic boundary conditions are imposed in both x and y-directions. Various values of Larmor radius $r_{L_i}=0,0.5,1.0,2.0$ are used in our calculation. The total density, total pressure, magnetic pressure, and total kinetic energy distributions at output times $t=0.5,2,3$ for $r_{L_i}=0$ is shown in Figs. 19-21. Fig. 22 shows the results for $r_{L_i}=1.0$ at $t=3$. In Fig. 23, we plot the pressure distribution along $y=0.625\pi$ for $r_{L_i}=1.0$ and $r_{L_i}=0$ cases, and compare the results of $r_{L_i}=0$ with the ideal MHD solution.

The magnetic reconnection happens near the center of the computational domain as shown in Fig. 24, which merges two 'magnetic rings' into a single one with the time evolution. The magnetic reconnection mechanism is different for different r_{L_i}, as shown in Fig. 24. For $r_{L_i}=0$ case, the aspect ratio of the reconnection layer is large where a double Y-point geometry is observed. In this case, the reconnection is driven by the magnetic diffusion, following the mechanism described by the Sweet-Parker model [40]. For $r_{L_i}=0.5,1.0$ cases, the Hall effect shows up and the length of reconnection layer gets shorter. Electron current sheet is observed along the reconnection layer. For $r_{L_i}=2.0$ case, the Hall effect becomes dominant and an X-point geometry is observed. The simulation

https://doi.org/10.4208/cicp.OA-2017-0102 Published online by Cambridge University Press

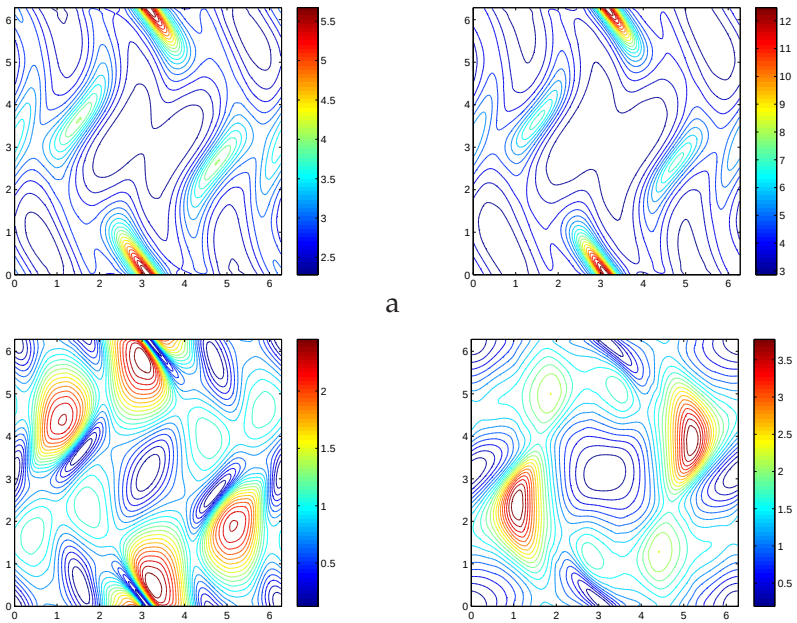


Figure 19: The Orszag-Tang MHD turbulence problem ($r_{L_i}=0$) with a uniform mesh of 192×192 grid points. The output time is $t=0.5$. (a) density; (b) gas pressure; (c) magnetic pressure; (d) kinetic energy.

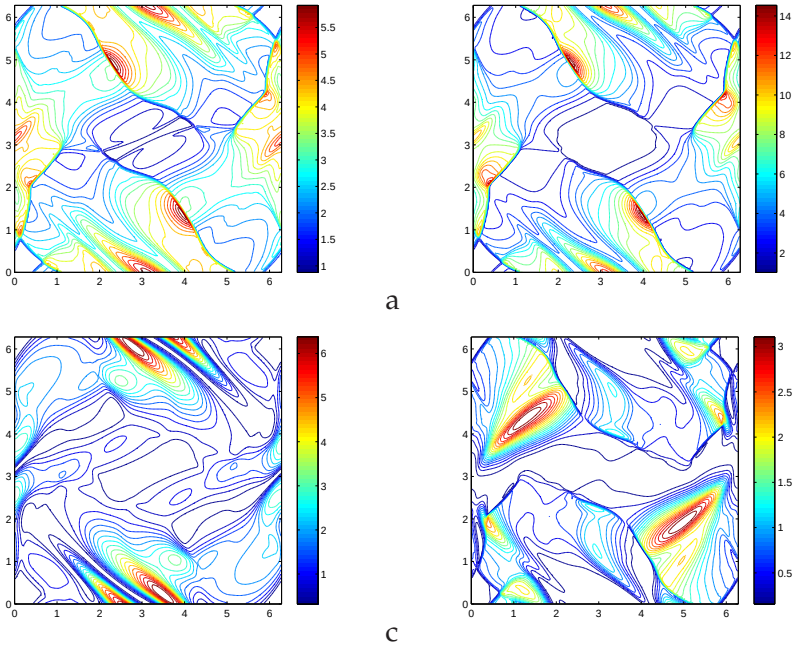


Figure 20: The Orszag-Tang MHD turbulence problem ($r_{L_i}=0$) at output time $t=2$. (a) density; (b) gas pressure; (c) magnetic pressure; (d) kinetic energy.

https://doi.org/10.4208/cicp.OA-2017-0102 Published online by Cambridge University Press

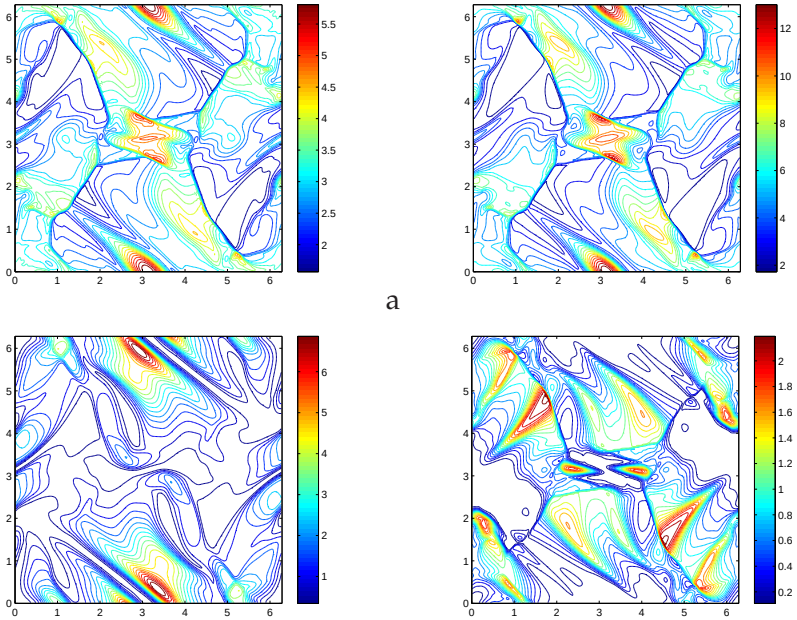


Figure 21: The Orszag-Tang MHD turbulence problem ($r_{L_i}=0$) at output time $t=3$. (a) density; (b) gas pressure; (c) magnetic pressure; (d) kinetic energy.

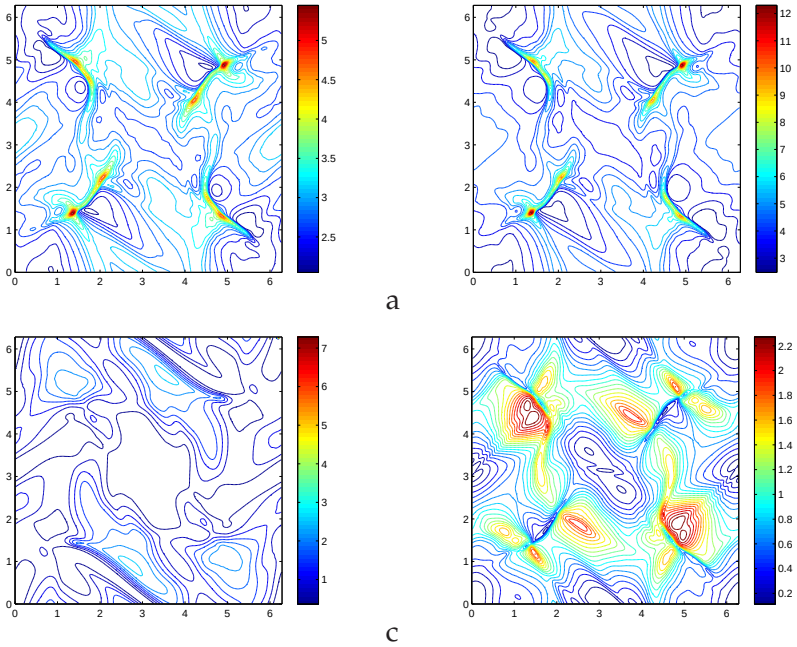


Figure 22: The Orszag-Tang MHD turbulence problem ($r_{L_i}=1.0$) at output time $t=3$. (a) density; (b) gas pressure; (c) magnetic pressure; (d) kinetic energy.

https://doi.org/10.4208/cicp.OA-2017-0102 Published online by Cambridge University Press

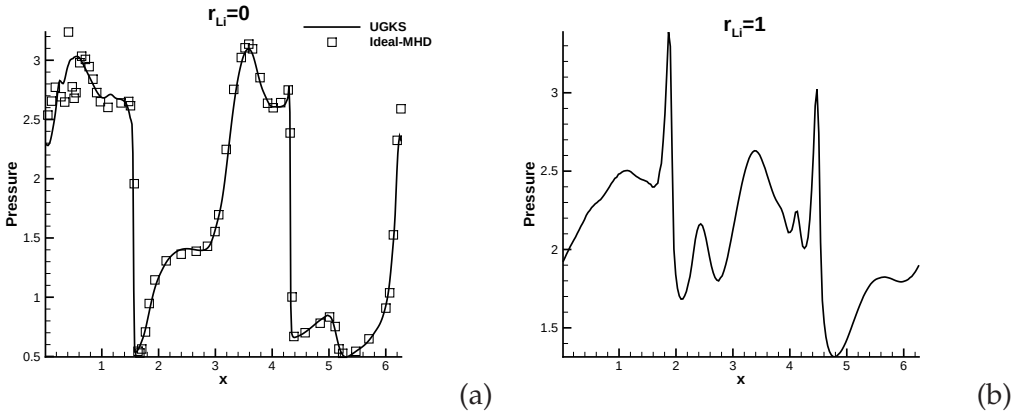


Figure 23: Pressure distribution along the line $y=0.625\pi$: (a) $r_{L_i}=0$, UGKS solution and ideal-MHD solution [39]. (b) $r_{L_i}=1.0$, UGKS solution only.

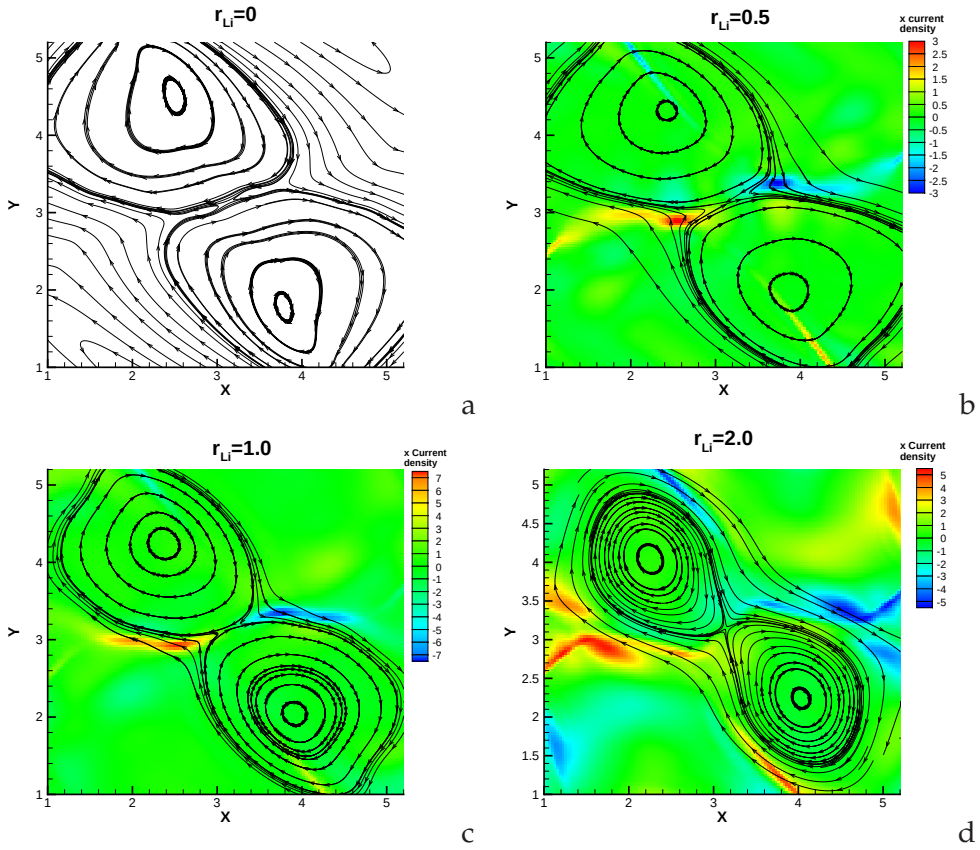


Figure 24: The topology of magnetic lines near the center of computational domain at $t=2$ with (a) $r_{L_i}=0$,(b) $r_{L_i}=0.5$,(c) $r_{L_i}=1.0$ and (d) $r_{L_i}=2.0$. The electron current sheets during the reconnection process are shown in (b), (c), and (d).

https://doi.org/10.4208/cicp.OA-2017-0102 Published online by Cambridge University Press

shows that the reconnection rate is increased with a higher energy transfer efficiency as r_{L_i} increases.

5.8 Magnetic reconnection

Magnetic reconnection is a process in which the topology of the magnetic field lines changes [41]. In ideal MHD, the magnetic field lines cannot be changed as the field lines are 'frozen' into the fluid. Various models were used to describe this phenomenon, for example the electron MHD [42], MHD and Hall MHD [43,44], full particle [45], and hybrid model [46]. It was found that the reconnection initiates at a length scale on the order of the electron skin depth and the reconnection rate is governed by the ion dynamics. Our scheme is based on the Vlasov-BGK equation which can describe the physics at electron skin depth level. Hence it can be used to describe the reconnection process.

The simulation uses the same initial conditions as the GEM challenge problem [17]. The initial magnetic field is given by

$$\mathbf{B}(y)=B_0\tanh(y/\lambda)\mathbf{e_x},$$

and a corresponding current sheet is carried by the electrons

$$\mathbf{J}_e=-\frac{B_0}{\lambda}\mathrm{sech}^2(y/\lambda)\mathbf{e_z}.$$

The initial number densities of electron and ion are

$$n_e=n_i=1/5+\mathrm{sech}^2(y/\lambda).$$

The electron and ion pressures are set to be

$$P_i=5P_e=\frac{5B_0}{12}n(y),$$

where $B_0=0.1$, $m_i=25m_e$ and $\lambda=0.5$. The electromagnetic correction potentials are set $\phi=\psi=0$ initially. The computational domain is $[-L_x/2,L_x/2]\times[-L_y/2,L_y/2]$ with $L_x=8\pi$, $L_y=4\pi$, which is divided into 200×100 cells. Periodic boundaries are applied at $x=\pm L_x/2$ and conducting wall boundaries at $y=\pm L_y/2$. To initiate reconnection, the magnetic field is perturbed with $\delta\mathbf{B}=\mathbf{e_z}\times\nabla_{\mathbf{x}}\psi$, where

$$\psi(x,y)=0.1B_0\cos(2\pi x/L_x)\cos(\pi y/L_y).$$

The velocity space for ion is $[-3,3]\times[-3,3]$ and for electron is $[-25,25]\times[-25,25]$ with 32×32 velocity grids. The computational time for UGKS is about 1342 mins on a 3.40GHz 4-core CPU.

Fig. 25 shows the reconnected flux of UGKS defined by

$$\phi(t)=\frac{1}{2L_x}\int_{-L_x/2}^{L_x/2}|B_y(x,0,t)|dx,$$

https://doi.org/10.4208/cicp.OA-2017-0102 Published online by Cambridge University Press

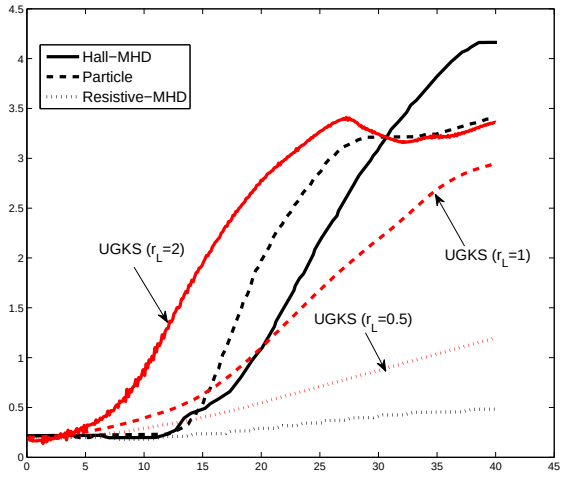


Figure 25: The reconnected flux $\phi(t)$ from the UGKS and other GEM simulations.

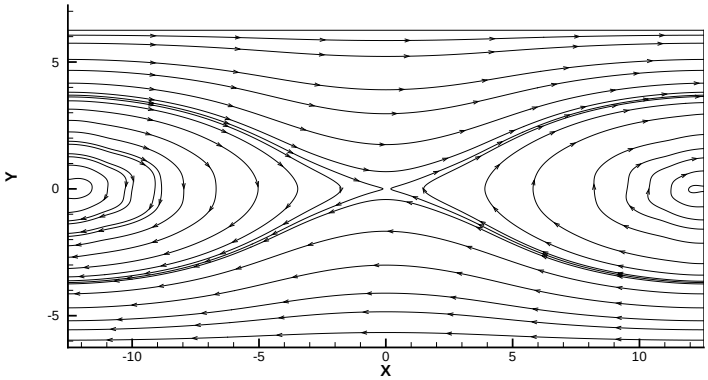


Figure 26: Magnetic flux at $\omega t = 40$ with $r_L = 1$.

which are compared with other GEM results. The fast reconnection rate can be predicted by UGKS, and the magnitude of reconnected flux depends on the plasma conditions. It can be observed from the results that the reconnected flux from UGKS behaves likes resistive-MHD result when the normalized Larmor radius is small ($r_L = 0.5$), and approaches to Hall-MHD solution when the normalized Larmor radius is large ($r_L = 2$). Fig. 26 shows the magnetic flux at $\omega t = 40$, with $r_L = 1$. Fig. 27 shows the electromagnetic and flow energy. The total energy of the system almost keeps a constant. The electron and ion densities, and momentum distribution at $t = 40\omega^{-1}$ are shown in Fig. 28, as well as the electromagnetic fields.

https://doi.org/10.4208/cicp.OA-2017-0102 Published online by Cambridge University Press

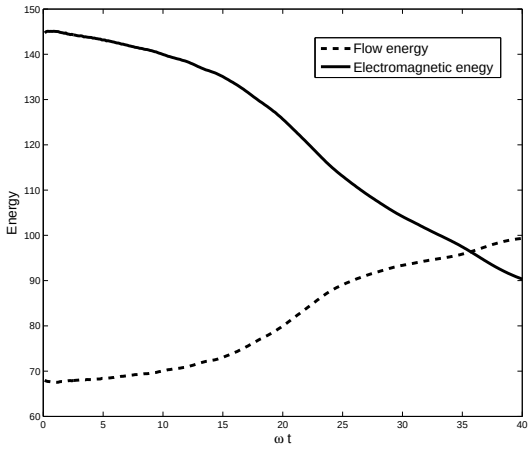


Figure 27: Electromagnetic and flow energy evolution in the magnetic reconnection process.

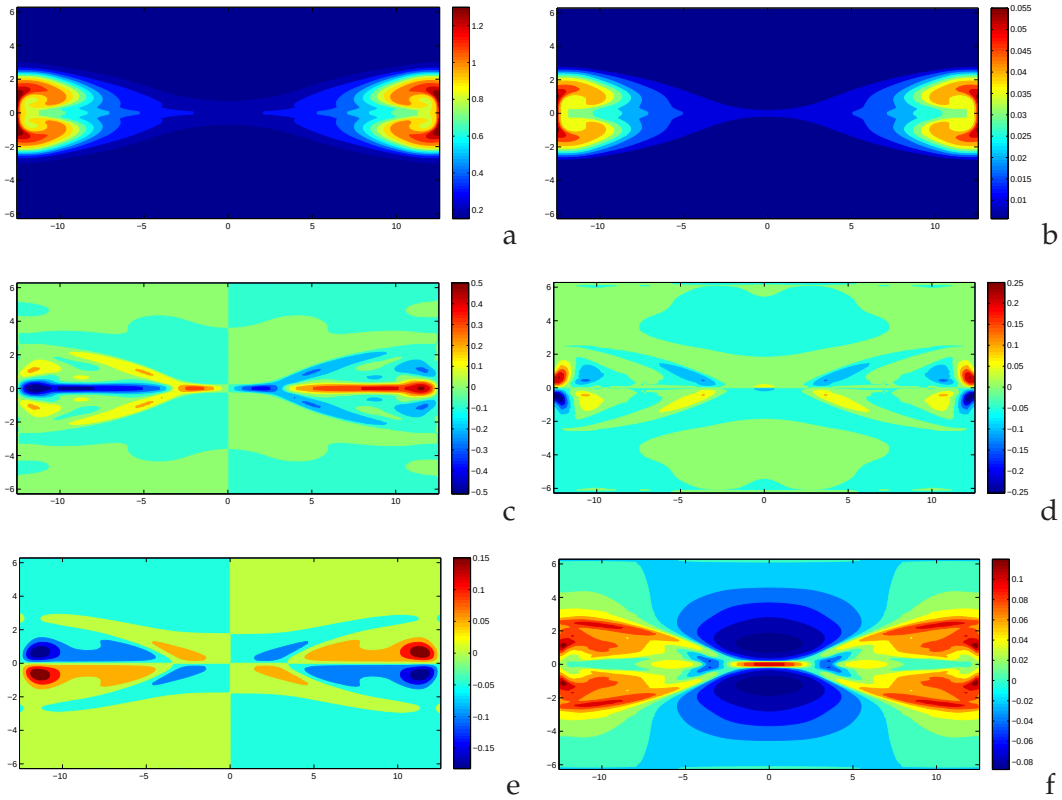


Figure 28: The reconnection process with $r_L = 1.0$ at $t = 40\omega^{-1}$. (a) ion density; (b) electron density; (c) x-directional electric current density; (d) y-directional electric current density; (e) z-direction magnetic field; (e) z-direction electric field.

https://doi.org/10.4208/cicp.OA-2017-0102 Published online by Cambridge University Press

6 Conclusion

In this paper, a multi-scale numerical method for multi-species plasma simulation in the whole flow regimes has been constructed. The UGKS takes into account the collisions among electrons and ions, and their coupling with the full Maxwell equations. The UGKS describes the plasma evolution on the mesh size and time step scales, which intrinsically provides the fundamental multi-scale discretized governing equations. The flow physics covered by the current scheme is more general than those from either the collisionless Vlasov equation or MHD equations in the corresponding kinetic or hydrodynamic limit alone. More importantly, the UGKS can give a reliable physical solution in the transitional regime as well, which has not been fully explored before from the particle-based and MHD-based numerical methods.

In the generalized Brio-Wu test case, the UGKS presents a smooth transition from neutral fluid results to the MHD solutions. At the same time, with the time evolution the results from the kinetic Vlasov equation and the solutions from the hydrodynamic two-fluid system have been recovered in the single UGKS formulation. The study of the Orszag-Tang turbulence problem shows the ability of the UGKS in capturing all kinds of MHD solutions and recovering the magnetic reconnection mechanism under different conditions. The UGKS is also able to capture the phenomena on the scale of Debye length, such as the fast magnetic reconnection in GEM case. The direct modeling methodology makes it possible to construct UGKS for the study of multi-scale transport in the rarefied gas dynamics, radiative transfer, and plasma physics.

Acknowledgments

The current work is supported by Hong Kong Research Grant Council (16211014, 16207715), HKUST research fund (PROVOST13SC01, IRS16SC42, SBI14SC11), and National Science Foundation of China (91330203, 91530319).

A Asymptotic limits of BGK-Maxwell system

A.1 Hydrodynamic two-fluid system in continuum regime

We study the asymptotic limit of nondimensional BGK-Maxwell system Eq. (2.11) in the regime where the nondimensional collision rate $\nu_{\alpha\alpha} \gg \max(1,\nu_{ie})$ for $\alpha = i,e$, equivalently the nondimensional relaxation parameter $\tau_\alpha \ll 1$. The velocity distribution function f_α and the post collision distribution function f_α^+ can be expanded as

$$\begin{aligned} f_\alpha^+ &= g_{\alpha 0} + \tau_\alpha g_{\alpha 1} + \mathcal{O}(\tau_\alpha^2), \\ f_\alpha &= f_{\alpha 0} + \tau_\alpha f_{\alpha 1} + \mathcal{O}(\tau_\alpha^2), \end{aligned} \tag{A.1}$$

https://doi.org/10.4208/cicp.OA-2017-0102 Published online by Cambridge University Press

where g_0 is the Maxwellian distribution with conservative moments

$$\int \Psi g_0 d\mathbf{u} = \lim_{\tau_\alpha \to 0} \overline{W}_\alpha = W_\alpha. \tag{A.2}$$

Substitute expansion Eq. (A.1) into Eq. (2.11), the balance of $\mathcal{O}(\tau_\alpha^{-1})$ terms give

$$f_{\alpha 0} = g_{\alpha 0}. \tag{A.3}$$

Therefore the zero-th order of the BGK equation is

$$\frac{\partial g_{\alpha 0}}{\partial t} + \mathbf{u}\cdot\nabla_{\mathbf{x}} g_{\alpha 0} + \frac{e}{r_{L_i} m_\alpha}(\mathbf{E}+\mathbf{u}\times\mathbf{B})\cdot\nabla_{\mathbf{u}} g_{\alpha 0} = \frac{f_\alpha^+ - g_{\alpha 0}}{\tau_\alpha}. \tag{A.4}$$

By taking conservative moments to Eq. (A.4), the hydrodynamic two-fluid Euler equations can be obtained [17].

A.2 Euler equations in nonconductive limit

The hydrodynamic two-fluid Euler equations converge to one fluid Euler equations in the nonconductive limit, when the interspecies collision rate is strong enough so that the electromagnetic waves cannot penetrate. In this regime $\nu_{ie}^{-1} \ll \min(1, r_{L_i})$, the flow velocity and temperature of ion can be expanded as

$$\begin{aligned} \mathbf{U}_i &= \mathbf{U}_{i0} + \nu_{ie}^{-1}\mathbf{U}_{i1} + \mathcal{O}(\nu_{ie}^{-2}), \\ T_i &= T_{i0} + \nu_{ie}^{-1} T_{i1} + \mathcal{O}(\nu_{ie}^{-2}). \end{aligned} \tag{A.5}$$

Substituting expansion Eq. (A.5) into the ion momentum equation in the two fluid Euler system, the balance of $\mathcal{O}(\nu_{ie})$ terms give

$$U_{i0} = U_e. \tag{A.6}$$

Then, the velocity difference of electron and ion is to the order of ν_{ie}^{-1}. The zero-th order w.r.t. $(r_{L_i}\nu_{ie})^{-1}$ of the two fluid momentum equation gives

$$\partial_t(\rho_\alpha \mathbf{U}) + \nabla_{\mathbf{x}}\cdot(\rho_\alpha \mathbf{U}\mathbf{U} + p_\alpha I) = 0, \tag{A.7}$$

where $\mathbf{U} = \mathbf{U}_{i0} = \mathbf{U}_{e0}$ is the common velocity. Substitute expansion Eq. (A.5) into the ion energy equation in the two fluid Euler system, the balance of $\mathcal{O}(\nu_{ie})$ terms gives

$$T_{i0} = T_{e0}. \tag{A.8}$$

Therefore, the ion and electron share the same temperature to the zero-th order of ν_{ie}^{-1}. In the limit $\nu_{ie} \to \infty$, the zero-th order of the two fluid system w.r.t $(r_{L_i}\nu_{ie})^{-1}$ gives the Euler equations for the total density, common velocity and temperature in Eq. (2.17).

https://doi.org/10.4208/cicp.OA-2017-0102 Published online by Cambridge University Press

A.3 General Ohm's law, Hall-MHD equations, and MHD equations

For a modest value of interspecies interaction coefficient ν_{ie}, the Hall effect or the separated motion of ions and electrons can take place. In such a case, the electron momentum equation can be written as

$$\mathbf{E}+\mathbf{U}_i\times\mathbf{B}=\frac{2r_{L_i}m_im_e\nu_{ie}}{(m_i+m_e)n_ee^2}\mathbf{j}+\frac{1}{n_ee}\mathbf{j}\times\mathbf{B}+\frac{r_{L_i}}{n_ee}\partial_t(\rho_e\mathbf{U}_e)+\frac{r_{L_i}}{n_ee}\nabla_{\mathbf{x}}\cdot(\rho_e\mathbf{U}_e\mathbf{U}_e+p_eI). \tag{A.9}$$

The first term on the righthand side is the electric resistivity, the second term corresponds to the Hall effect, the last two term corresponds to the effect of electron inertia and pressure. We write the center-of-mass velocity as $\mathbf{U}$,

$$\mathbf{U}=\frac{m_i\mathbf{U}_i+m_e\mathbf{U}_e}{m_i+m_e}. \tag{A.10}$$

In the limit $m_e/m_i\ll 1$, we have

$$\begin{aligned}\mathbf{U}_i&=\mathbf{U}+\mathcal{O}\Big(\frac{m_e}{m_i}\Big),\\ \mathbf{U}_e&=\mathbf{U}-\frac{\mathbf{j}}{ne}+\mathcal{O}\Big(\frac{m_e}{m_i}\Big).\end{aligned} \tag{A.11}$$

In the limit $\lambda_D\sim c^{-1}\ll 1$, the Ampère's law becomes

$$\mathbf{j}=r_{L_i}\lambda_D^2c^2\nabla_{\mathbf{x}}\times\mathbf{B}+\mathcal{O}(U_0^2/c^2), \tag{A.12}$$

where the displacement current is to the order of the square of ratio between the reference velocity to the speed of light. The above low frequency Ampère's law indicates that $\nabla\cdot\mathbf{j}=0$, and therefore in this regime, the plasma is quasi-neutral, namely $n_i\approx n_e$. In the limit $m_e/m_i\to 0$ and $\lambda_D\sim c^{-1}\to 0$, the electron momentum equation gives the generalized Ohm's law

$$E+\mathbf{U}\times B=\frac{r_{L_i}}{\sigma}\mathbf{j}+\frac{1}{n_ee}\mathbf{j}\times\mathbf{B}+\frac{r_{L_i}}{n_ee}\nabla_{\mathbf{x}}p_e. \tag{A.13}$$

In such regime, the two fluid equations reduce to one fluid Hall-MHD equations (2.19).

The Hall term and the electron pressure term are on the order of Larmor radius. In the limit $r_{L_i}\to 0$, both the current density and the electric pressure term converge to zero, and the generalized Ohm's law reduces to the ideal Ohm's law

$$\mathbf{E}+\mathbf{U}\times\mathbf{B}=0. \tag{A.14}$$

Substituting Eq. (A.14) into Eq. (2.19), the ideal-MHD equations Eq. (2.20) can be obtained, which is valid in the highly collisional and highly magnetized regime.

https://doi.org/10.4208/cicp.OA-2017-0102 Published online by Cambridge University Press

B Eigen-system of perfectly hyperbolic Maxwell equations

The PHM equations [36] read

$$\frac{\partial \mathbf{Q}}{\partial t}+\mathbf{A}_1\frac{\partial \mathbf{Q}}{\partial x}+\mathbf{A}_2\frac{\partial \mathbf{Q}}{\partial y}=s, \tag{B.1}$$

where $\mathbf{Q}=(E_1,E_2,E_3,B_1,B_2,B_3,\phi,\psi)^T$, $\mathbf{s}=(-J_1/\epsilon,-J_2/\epsilon,-J_3/\epsilon,0,0,0,\chi\rho/\epsilon_0,0)^T$,

$$A_1=\begin{pmatrix} 0 & 0 & 0 & 0 & 0 & 0 & c^2\chi & 0\\ 0 & 0 & 0 & 0 & 0 & c^2 & 0 & 0\\ 0 & 0 & 0 & 0 & -c^2 & 0 & 0 & 0\\ 0 & 0 & 0 & 0 & 0 & 0 & 0 & \nu\\ 0 & 0 & -1 & 0 & 0 & 0 & 0 & 0\\ 0 & 1 & 0 & 0 & 0 & 0 & 0 & 0\\ \chi & 0 & 0 & 0 & 0 & 0 & 0 & 0\\ 0 & 0 & 0 & c^2\nu & 0 & 0 & 0 & 0 \end{pmatrix},$$

and

$$A_2=\begin{pmatrix} 0 & 0 & 0 & 0 & 0 & -c^2 & 0 & 0\\ 0 & 0 & 0 & 0 & 0 & 0 & c^2\chi & 0\\ 0 & 0 & 0 & c^2 & 0 & 0 & 0 & 0\\ 0 & 0 & 1 & 0 & 0 & 0 & 0 & 0\\ 0 & 0 & 0 & 0 & 0 & 0 & 0 & \nu\\ -1 & 0 & 0 & 0 & 0 & 0 & 0 & 0\\ 0 & \chi & 0 & 0 & 0 & 0 & 0 & 0\\ 0 & 0 & 0 & 0 & c^2\nu & 0 & 0 & 0 \end{pmatrix}.$$

For A_1, the eigenvalues are $\{c,c,c\chi,c\nu,-c,-c,-c\chi,-c\nu\}$. The right eigenvectors of A_1 are given by the columns of the matrix

$$R_1=\begin{pmatrix} 0 & 0 & c & 0 & 0 & 0 & -c & 0\\ 0 & c & 0 & 0 & 0 & -c & 0 & 0\\ -c & 0 & 0 & 0 & c & 0 & 0 & 0\\ 0 & 0 & 0 & 1/c & 0 & 0 & 0 & -1/c\\ 1 & 0 & 0 & 0 & 1 & 0 & 0 & 0\\ 0 & 1 & 0 & 0 & 0 & 1 & 0 & 0\\ 0 & 0 & 1 & 0 & 0 & 0 & 1 & 0\\ 0 & 0 & 0 & 1 & 0 & 0 & 0 & 1 \end{pmatrix}.$$

https://doi.org/10.4208/cicp.OA-2017-0102 Published online by Cambridge University Press

The left eigenvectors are the rows of the matrix

$$L_1=\begin{pmatrix} 0 & 0 & -\frac{1}{2c} & 0 & \frac{1}{2} & 0 & 0 & 0 \\ 0 & \frac{1}{2c} & 0 & 0 & \frac{1}{2} & 0 & 0 & 0 \\ \frac{1}{2c} & 0 & 0 & 0 & 0 & 0 & \frac{1}{2} & 0 \\ 0 & 0 & 0 & 0 & \frac{c}{2} & 0 & 0 & \frac{1}{2} \\ 0 & 0 & \frac{1}{2c} & 0 & \frac{1}{2} & 0 & 0 & 0 \\ 0 & -\frac{1}{2c} & 0 & 0 & \frac{1}{2} & 0 & 0 & 0 \\ -\frac{1}{2c} & 0 & 0 & 0 & 0 & 0 & \frac{1}{2} & 0 \\ 0 & 0 & 0 & 0 & -\frac{c}{2} & 0 & 0 & \frac{1}{2} \end{pmatrix}.$$

For A_2, the eigenvalues are $\{c,c,c\chi,c\nu,-c,-c,-c\chi,-c\nu\}$. The right eigenvectors of A_2 are given by the columns of the matrix

$$R_2=\begin{pmatrix} 0 & -c & 0 & 0 & 0 & c & 0 & 0 \\ 0 & 0 & c & 0 & 0 & 0 & -c & 0 \\ c & 0 & 0 & 0 & -c & 0 & 0 & 0 \\ 1 & 0 & 0 & 0 & 1 & 0 & 0 & 0 \\ 0 & 0 & 0 & 1/c & 0 & 0 & 0 & -1/c \\ 0 & 1 & 0 & 0 & 0 & 1 & 0 & 0 \\ 0 & 0 & 1 & 0 & 0 & 0 & 1 & 0 \\ 0 & 0 & 0 & 1 & 0 & 0 & 0 & 1 \end{pmatrix}.$$

The left eigenvectors are the rows of the matrix

$$L_2=\begin{pmatrix} 0 & 0 & \frac{1}{2c} & \frac{1}{2} & 0 & 0 & 0 & 0 \\ -\frac{1}{2c} & 0 & 0 & 0 & 0 & \frac{1}{2} & 0 & 0 \\ 0 & \frac{1}{2c} & 0 & 0 & 0 & 0 & \frac{1}{2} & 0 \\ 0 & 0 & 0 & 0 & \frac{c}{2} & 0 & 0 & \frac{1}{2} \\ 0 & 0 & -\frac{1}{2c} & \frac{1}{2} & 0 & 0 & 0 & 0 \\ \frac{1}{2c} & 0 & 0 & 0 & 0 & \frac{1}{2} & 0 & 0 \\ 0 & -\frac{1}{2c} & 0 & 0 & 0 & 0 & \frac{1}{2} & 0 \\ 0 & 0 & 0 & 0 & -\frac{c}{2} & 0 & 0 & \frac{1}{2} \end{pmatrix}.$$

C Numerical flux for the reduced distribution function and the update of reduced distribution function

In this appendix, we present the numerical flux for reduced distribution function and the update of reduced velocity distribution function due to Lorenz acceleration and collision. The two dimensional problems are considered with three reduced distribution functions introduced in Eq. (5.4), the subscript α is omitted in this appendix.

https://doi.org/10.4208/cicp.OA-2017-0102 Published online by Cambridge University Press

C.1 Numerical flux for the reduced distribution function

The numerical flux for the reduced distribution function can be obtained by taking corresponding moments and time integration to the integral solution of BGK equation (3.22). Denoting the time integration by

$$
\begin{aligned}
&Mt_1=\tau e^{-\Delta t/\tau}+\Delta t-\tau, \quad Mt_2=\tau\left(-e^{-\Delta t}\tau(\Delta t+2\tau)-\Delta t+2\tau\right),\\
&Mt_3=\left(-\tau^2e^{-\Delta t/\tau}+\Delta t^2/2-\tau\Delta t+\tau^2\right), \quad Mt_4=\tau\left(1-e^{-\Delta t/\tau}\right),\\
&Mt_5=\tau\left(e^{-\Delta t/\tau}(\Delta t+\tau)-\tau\right).
\end{aligned}
$$

The numerical flux for h_0, h_1 and h_2 are

$$
\begin{aligned}
F_{h_0,i-1/2}=&\int_0^{\Delta t}\int uf(x_{i-1/2},y_j,t,u_p,v_q,w_r)dwdt\\
=&Mt_1uH_0+Mt_2u^2H(u)\left(\mathbf{a}_x^L\cdot\left(1,u,v,0,\frac{1}{2}(u^2+v^2)\right)H_0+a_{x,4}^LH_1+\frac{1}{2}a_{x,5}^LH_2\right)\\
&+Mt_2u^2(1-H[u])\left(\mathbf{a}_x^R\cdot\left(1,u,v,0,\frac{1}{2}(u^2+v^2)\right)H_0+a_{x,4}^RH_1+\frac{1}{2}a_{x,5}^RH_2\right)\\
&+Mt_2uv\left(\mathbf{a}_y\cdot\left(1,u,v,0,\frac{1}{2}(u^2+v^2)\right)H_0+a_x^4H_1+\frac{1}{2}a_x^5H_2\right)\\
&-Mt_2u(l_1\lambda(u-U)H_0+l_2\lambda(v-V)H_0)\\
&+Mt_3u\left(\mathbf{A}\cdot\left(1,u,v,0,\frac{1}{2}(u^2+v^2)\right)H_0+A^4H_1+\frac{1}{2}A^5H_2\right)\\
&+Mt_4u(h_0^LH[u]+H_0^L(1-H[u]))\\
&-Mt_5H[u](u^2h_{0x}^L+uvh_{0y}^L+ul_1f_{0u}^L+vl_2f_{0v}^L)\\
&-Mt_5(1-H[u])(u^2h_{0x}^R+uvh_{0y}^R+ul_1f_{0u}^R+vl_2f_{0v}^R),
\end{aligned}
\tag{C.1}
$$

$$
\begin{aligned}
F_{h_1,i-1/2}=&\int_0^{\Delta t}\int uwf(x_{i-1/2},y_j,t,u_p,v_q,w_r)dwdt\\
=&Mt_1uH_1+Mt_2u^2H[u]\left(\mathbf{a}_x^L\cdot\left(1,u,v,0,\frac{1}{2}(u^2+v^2)\right)H_1+a_{x,4}^LH_2+\frac{1}{2}a_{x,5}^L<w^3>H_0\right)\\
&+Mt_2u^2(1-H[u])\left(\mathbf{a}_x^R\cdot\left(1,u,v,0,\frac{1}{2}(u^2+v^2)\right)H_1+a_{x,4}^RH_2+\frac{1}{2}a_{x,5}^R<w^3>H_0\right)\\
&+Mt_2uv\left(\mathbf{a}_y\cdot\left(1,u,v,0,\frac{1}{2}(u^2+v^2)\right)H_1+a_x^4H_2+\frac{1}{2}a_x^5<w^3>H_0\right)\\
&-Mt_2u(l_1\lambda(u-U)H_1+l_2\lambda(v-V)H_1+l_3H_0)
\end{aligned}
$$

https://doi.org/10.4208/cicp.OA-2017-0102 Published online by Cambridge University Press

$$
\begin{aligned}
&+Mt_3u\left(\mathbf{A}\cdot\left(1,u,v,0,\frac{1}{2}(u^2+v^2)\right)H_1+A^4H_2+\frac{1}{2}A^5<w^3>H_0\right)\\
&+Mt_4u(h_1^LH[u]+H_1^L(1-H[u]))\\
&-Mt_5H[u](u^2h_{1x}^L+uvh_{0y}^L+ul_1f_{1u}^L+vl_2f_{1v}^L-l_3h_0)\\
&-Mt_5(1-H[u])(u^2h_{1x}^R+uvh_{1y}^R+ul_1f_{1u}^R+vl_2f_{1v}^R-l_3h_0),
\end{aligned}\tag{C.2}
$$

$$
\begin{aligned}
F_{h_2,i-1/2}=&\int_0^{\Delta t}\int uw^2f(x_{i-1/2},y_j,t,u_p,v_q,w_r)dwdt\\
=&Mt_1uH_2+Mt_2u^2H(u)\left(\mathbf{a}_x\cdot\left(1,u,v,0,\frac{1}{2}(u^2+v^2)\right)H_2\right.\\
&\left.+a_{x,4}^L<w^3>H_0+\frac{1}{2}a_{x,5}^L<w^4>H_0\right)\\
&+Mt_2u^2(1-H[u])\left(\mathbf{a}_x^R\cdot\left(1,u,v,0,\frac{1}{2}(u^2+v^2)\right)H_2\right.\\
&\left.+a_{x,4}^R<w^3>H_0+\frac{1}{2}a_{x,5}^R<w^4>H_0\right)\\
&+Mt_2uv\left(\mathbf{a}_y\cdot\left(1,u,v,0,\frac{1}{2}(u^2+v^2)\right)H_2+a_x^4<w^3>H_0+\frac{1}{2}a_x^5<w^4>H_0\right)\\
&-Mt_2u(l_1\lambda(u-U)H_2+l_2\lambda(v-V)H_2+l_3H_1)\\
&+Mt_3u\left(\mathbf{A}\cdot\left(1,u,v,0,\frac{1}{2}(u^2+v^2)\right)H_2+A^4<w^3>H_0+\frac{1}{2}A^5<w^4>H_0\right)\\
&+Mt_4u(h_2^LH[u]+H_2^L0(1-H[u]))\\
&-Mt_5H[u](u^2h_{2x}^L+uvh_{2y}^L+ul_1f_{2u}^L+vl_2f_{2v}^L-2l_3h_1)\\
&-Mt_5(1-H[u])(u^2h_{2x}^R+uvh_{2y}^R+ul_1f_{2u}^R+vl_2f_{2v}^R-2l_3h_1).
\end{aligned}\tag{C.3}
$$

And the numerical flux for **W** is

$$
\begin{aligned}
\mathbf{F}_{w,i-1/2}=&Mt_1\rho_0<u\phi>+Mt_2\rho_0(<a_xu^2\phi>+<a_yuv\phi>)+Mt_3\rho_0<Au\phi>\\
&-Mt_2\rho_0\begin{pmatrix}l_1\\2l_1U_0\\l_1V_0+l_2U_0\\l_1V_0+l_3U_0\\l_1(3U_0^2+V_0^2+W_0^2)/2+l_2U_0V_0+l_3U_0W_0+\frac{5l_1}{4\lambda}\end{pmatrix}\\
&+Mt_4\begin{pmatrix}\sum\omega uh_0\\\sum\omega u^2h_0\\\sum\omega uvh_0\\\sum\omega uh_1\\\frac{1}{2}\sum\omega u((u^2+v^2)h_0+h_2)\end{pmatrix}
\end{aligned}
$$

https://doi.org/10.4208/cicp.OA-2017-0102 Published online by Cambridge University Press

$$
\begin{aligned}
&-Mt_5\begin{pmatrix}
\sum\omega(u^2h_x+uvh_y)\\
\sum\omega(u^3h_x+u^2vh_y)\\
\sum\omega(u^2vh_x+uv^2h_y)\\
\sum\omega(u^2h_{1x}+uvh_{1y})\\
\frac{1}{2}\sum\omega((u^2+v^2)(u^2h_x+uvh_y)+u^2h_{2x}+uvh_{2y})
\end{pmatrix}\\
&+Mt_5\begin{pmatrix}
\sum\omega(2l_1uh_0)\\
\sum\omega(3l_1u^2h_0)\\
\sum\omega(2l_1uvh_0)\\
\sum\omega(2l_1uh_1)\\
\frac{1}{2}\sum\omega(2u(u^2+v^2)h_0+2uh_2+3u^2u(h_0+h_1))
\end{pmatrix},
\end{aligned}
\tag{C.4}
$$

where $<\cdots>$ is the moments of equilibrium distribution function and $\sum$ is the summation over all velocity points with the weighting function ω.

C.2 Update of the reduced distribution function

Based the exact solution Eq. (3.28), firstly the distribution functions is shifted as

$$
\begin{aligned}
h_0^{**}(u_k,v_l)&=h_0^*(u_{k-su},v_{l-sv})\mathrm{e}^{-\Delta t_1/\tau}+(H_0^*(u_{k-su},v_{l-sv}))(1-\mathrm{e}^{-\Delta t_1/\tau}),\\
h_1^{**}(u_k,v_l)&=h_1^*(u_{k-su},v_{l-sv})\mathrm{e}^{-\Delta t_1/\tau}+(H_1^*(u_{k-su},v_{l-sv})+\tau l_3h_0^*)(1-\mathrm{e}^{-\Delta t_1/\tau}),\\
h_2^{**}(u_k,v_l,w_m)&=h_2^*(u_{k-su},v_{l-sv})\mathrm{e}^{-\Delta t_1/\tau}+(H_2^*(u_{k-su},v_{l-sv})+2\tau l_3h_1^*)(1-\mathrm{e}^{-\Delta t_1/\tau}),
\end{aligned}
\tag{C.5}
$$

where the post-collision distribution H_0^*, H_1^*, H_2^* are obtained from $\overline{\mathbf{W}}^*$ in Eq. (3.29), and $su=\Delta t_1 l_u/\Delta u$, $sv=\Delta t_1 l_v/\Delta v$,

$$
\Delta t_1=\min\left(\frac{\Delta u}{|l_u|}\left\lfloor\frac{|l_u|\Delta t}{\Delta u}\right\rfloor,\frac{\Delta v}{|l_v|}\left\lfloor\frac{|l_v|\Delta t}{\Delta v}\right\rfloor\right).
$$

Then the distribution function is updated to the next time step as shown in Fig. 5-ii by

$$
\begin{aligned}
h_0^{n+1}&=\left(h_0^{**}-\sum_{s_j\in\partial\Omega_{\mathbf{v}j}}|s_j|\int_{t^n+\Delta t_1}^{t^{n+1}}\boldsymbol{\ell}\cdot\mathbf{n}h_0(\mathbf{x}_i,t,\mathbf{u}_{k+1/2})dt+\frac{\Delta t}{\tau^{n+1}}H_0^{n+1}\right)\Big/\left(1+\frac{\Delta t}{\tau^{n+1}}\right),\\
h_1^{n+1}&=\left(h_1^{**}-\sum_{s_j\in\partial\Omega_{\mathbf{v}j}}|s_j|\int_{t^n+\Delta t_1}^{t^{n+1}}\boldsymbol{\ell}\cdot\mathbf{n}h_1(\mathbf{x}_i,t,\mathbf{u}_{k+1/2})dt+\Delta tl_3h_0^{n+1}+\frac{\Delta t}{\tau^{n+1}}H_1^{n+1}\right)\Big/\left(1+\frac{\Delta t}{\tau^{n+1}}\right),\\
h_2^{n+1}&=\left(h_2^{**}-\sum_{s_j\in\partial\Omega_{\mathbf{v}j}}|s_j|\int_{t^n+\Delta t_1}^{t^{n+1}}\boldsymbol{\ell}\cdot\mathbf{n}h_2(\mathbf{x}_i,t,\mathbf{u}_{k+1/2})dt+2\Delta tl_3h_1^{n+1}+\frac{\Delta t}{\tau^{n+1}}H_2^{n+1}\right)\Big/\left(1+\frac{\Delta t}{\tau^{n+1}}\right),
\end{aligned}
\tag{C.6}
$$

https://doi.org/10.4208/cicp.OA-2017-0102 Published online by Cambridge University Press

where H_0^{n+1}, H_1^{n+1}, H_2^{n+1} and τ^{n+1} are obtained from the updated conservative variables $\overline{\mathbf{W}}$. As $t^{n+1}-t^n-\Delta t_1$ is smaller than the relaxation time τ, the simplified upwind flux can be used in Eq. (C.6),

$$h_i(\mathbf{x}_i,t,\mathbf{u}_{k+1/2})=h_i(\mathbf{x}_i,t^n+\Delta t_1,\mathbf{u}_{k+1/2}), \tag{C.7}$$

for $i=0,1,2$.

References

[1] National Research Council, *Plasma science: advancing knowledge in the national interest*. National Academies Press (2008).

[2] F. F. Chen, *Introduction to plasma physics and controlled fusion*. Plenum Press, New York and London, 2nd edition (1974).

[3] V. Vahedi and M. Surendra, "A Monte Carlo collision model for the particle-in-cell method: applications to argon and oxygen discharges," *Comput. Phys. Commun.*, vol. 87 (1995), no. 1, pp. 179–198.

[4] F. Filbet and E. Sonnendrücker, "Comparison of Eulerian Vlasov solvers," *Comput. Phys. Commun.*, vol. 150 (2003), no. 3, pp. 247–266.

[5] F. Filbet, E. Sonnendrücker, and P. Bertrand, "Conservative numerical schemes for the Vlasov equation," *J. Comput. Phys.*, vol. 172 (2001), no. 1, pp. 166–187.

[6] P. Degon, F. Deluzet, F. Navoret, and A.B. Sun, "Asymptotic-preserving particle-in-cell method for the VlasovCPoisson system near quasineutrality," *J. Comput. Phys.*, vol. 229 (2010), no. 1, pp. 5630–5652.

[7] P. Degon, F. Deluzet, F. Navoret, and A.B. Sun, "Asymptotic-preserving particle-in-cell method for the VlasovCMaxwell system in the quasi-neutral limit," *J. Comput. Phys.*, vol. 330 (2017), no. 1, pp. 467-492.

[8] P. Degon, F. Deluzet, "Asymptotic-Preserving methods and multiscale models for plasma physics," *arXiv preprint*, (2016).

[9] J.-M. Qiu and C.-W. Shu, "Conservative semi-Lagrangian finite difference WENO formulations with applications to the Vlasov equation," *Commun. Comput. Phys.*, vol. 10 (2011), no. 4, p. 979.

[10] W. Guo and J.-M. Qiu, "Hybrid semi-Lagrangian finite element-finite difference methods for the Vlasov equation," *J. Comput. Phys.*, vol. 234 (2013), pp. 108–132.

[11] T. Xiong, J.-M. Qiu, Z. Xu, and A. Christlieb, "High order maximum principle preserving semi-Lagrangian finite difference WENO schemes for the Vlasov equation," *J. Comput. Phys.*, vol. 273 (2014), pp. 618–639.

[12] K. G. Powell, P. L. Roe, T. J. Linde, T. I. Gombosi, and D. L. De Zeeuw, "A solution-adaptive upwind scheme for ideal magnetohydrodynamics," *J. Comput. Phys.*, vol. 154 (1999), no. 2, pp. 284–309.

[13] M. Brio and C. C. Wu, "An upwind differencing scheme for the equations of ideal magnetohydrodynamics," *J. Comput. Phys.*, vol. 75 (1988), no. 2, pp. 400–422.

[14] K. Xu, "Gas-kinetic theory-based flux splitting method for ideal magnetohydrodynamics," *J. Comput. Phys.*, vol. 153 (1999), no. 2, pp. 334–352.

[15] D. B. Araya, F. H. Ebersohn, S. E. Anderson, and S. S. Girimaji, "Magneto-gas kinetic method for nonideal magnetohydrodynamics flows: verification protocol and plasma jet simulations," *J. Fluids Eng.*, vol. 137 (2015), no. 8, p. 081302.

https://doi.org/10.4208/cicp.OA-2017-0102 Published online by Cambridge University Press

[16] U. Shumlak and J. Loverich, "Approximate Riemann solver for the two-fluid plasma model," *J. Comput. Phys.*, vol. 187 (2003), no. 2, pp. 620–638.
[17] A. Hakim, J. Loverich, and U. Shumlak, "A high resolution wave propagation scheme for ideal two-fluid plasma equations," *J. Comput. Phys.*, vol. 219 (2006), no. 1, pp. 418–442.
[18] J. Loverich and U. Shumlak, "A discontinuous Galerkin method for the full two-fluid plasma model," *J. Comput. Phys.*, vol. 169 (2005), no. 1, pp. 251–255.
[19] J. Loverich, A. Hakim, and U. Shumlak, "A discontinuous Galerkin method for ideal two-fluid plasma equations," *J. Comput. Phys.*, vol. 9 (2011), no. 02, pp. 240–268.
[20] B. Srinivasan and U. Shumlak, "Analytical and computational study of the ideal full two-fluid plasma model and asymptotic approximations for Hall-magnetohydrodynamics," *Phys. Plasmas*, vol. 18 (2011), no. 9, p. 092113.
[21] A. Crestetto, N. Crouseilles, and M. Lemou, "Kinetic/fluid micro-macro numerical schemes for Vlasov-Poisson-BGK equation using particles," *Kin. Rel. Mod.*, vol. 5 (2012), no. 4, pp. 787–816.
[22] G. Dimarco, L. Mieussens, and V. Rispoli, "An asymptotic preserving automatic domain decomposition method for the Vlasov-Poisson-BGK system with applications to plasmas," *J. Comput. Phys.*, vol. 274 (2014), pp. 122–139.
[23] S. Jin and B. Yan, "A class of asymptotic-preserving schemes for the Fokker-Planck-Landau equation," *J. Comput. Phys.*, vol. 230 (2011), no. 17, pp. 6420–6437.
[24] G. Dimarco, Q. Li, L. Pareschi, and B. Yan, "Numerical methods for plasma physics in collisional regimes," *J. Plasma Phys.*, vol. 81 (2015), no. 1, 305810106
[25] P. Degond, F. Deluzet, L. Navoret, A.-B. Sun, and M.-H. Vignal, "Asymptotic-preserving particle-in-cell method for the Vlasov–Poisson system near quasineutrality," *J. Comput. Phys.*, vol. 229 (2010), no. 16, pp. 5630–5652.
[26] K. Xu and J. Huang, "A unified gas-kinetic scheme for continuum and rarefied flows," *J. Comput. Phys.*, vol. 229 (2010), no. 20, pp. 7747–7764.
[27] J. Huang, K. Xu, and P. Yu, "A unified gas-kinetic scheme for continuum and rarefied flows II: Multi-dimensional cases," *Commun. Comput. Phys.*, vol. 12 (2012), no. 3, pp. 662–690.
[28] J. Huang, K. Xu, and P. Yu, "A unified gas-kinetic scheme for continuum and rarefied flows III: Microflow simulations," *Commun. Comput. Phys.*, vol. 14 (2013), no. 5, pp. 1147–1173.
[29] W. Sun, S. Jiang, and K. Xu, "An asymptotic preserving unified gas kinetic scheme for gray radiative transfer equations," *J. Comput. Phys.*, vol. 285 (2015), pp. 265–279.
[30] W. Sun, S. Jiang, K. Xu, and S. Li, "An asymptotic preserving unified gas kinetic scheme for frequency-dependent radiative transfer equations," *J. Comput. Phys.*, vol. 302 (2015), pp. 222–238.
[31] Z. Guo and K. Xu, "Discrete unified gas kinetic scheme for multiscale heat transfer based on the phonon Boltzmann transport equation," *Int. J. Heat Mass*, vol. 102 (2016), pp. 944–958.
[32] K. Xu, "Direct modeling for computational fluid dynamics: construction and application of unified gas-kinetic schemes," *World Scientific, Singapore* (2015).
[33] P. Andries, K. Aoki, and B. Perthame, "A consistent BGK-type model for gas mixtures," *J. Stat. Phys.*, vol. 106 (2002), no. 5-6, pp. 993–1018.
[34] T.F. Morse, "Energy and momentum exchange between nonequipartition gases," *Phys. Fluids*, vol. 6 (1963), no. 10, pp. 1420-1427.
[35] C. Liu, K. Xu, Q. Sun, and Q. Cai, "A unified gas-kinetic scheme for continuum and rarefied flows IV: full Boltzmann and model equations," *J. Comput. Phys.*, vol. 314 (2016), pp. 305–340.
[36] C.-D. Munz, P. Omnes, R. Schneider, E. Sonnendrücker, and U. Voss, "Divergence correction techniques for Maxwell solvers based on a hyperbolic model," *J. Comput. Phys.*, vol. 161

https://doi.org/10.4208/cicp.OA-2017-0102 Published online by Cambridge University Press

(2000), no. 2, pp. 484–511.
[37] R.J. LeVeque, " Finite volume methods for hyperbolic problems," *Cambridge university press* (2002).
[38] S. A. Orszag and C.-M. Tang, "Small-scale structure of two-dimensional magnetohydrodynamic turbulence," *J. Fluid Mech.*, vol. 90 (1979), no. 01, pp. 129–143.
[39] H.-Z. Tang and K. Xu, "A high-order gas-kinetic method for multidimensional ideal magnetohydrodynamics," *J. Comput. Phys.*, vol. 165 (2000), no. 1, pp. 69–88.
[40] E.N. Parker, "Sweet's mechanism for merging magnetic fields in conducting fluids," *J. Geophys. Res.*, vol. 62 (1957), no. 4, pp. 509–520.
[41] J. Birn, J. Drake, M. Shay, B. Rogers, R. Denton, M. Hesse, M. Kuznetsova, Z. Ma, A. Bhattacharjee, A. Otto, *et al.*, "Geospace environmental modeling (GEM) magnetic reconnection challenge," *J. Geophys. Res.-Space*, vol. 106 (2001), no. A3, pp. 3715–3719.
[42] M. Hesse, J. Birn, and M. Kuznetsova, "Collisionless magnetic reconnection: Electron processes and transport modeling," *J. Geophys. Res.-Space*, vol. 106 (2001), no. A3, pp. 3721–3735.
[43] J. Birn and M. Hesse, "Geospace environment modeling (GEM) magnetic reconnection challenge: Resistive tearing, anisotropic pressure and hall effects," *J. Geophys. Res.-Space*, vol. 106 (2001), no. A3, pp. 3737–3750.
[44] Z. Ma and A. Bhattacharjee, "Hall magnetohydrodynamic reconnection: The geospace environment modeling challenge," *J. Geophys. Res.-Space*, vol. 106 (2001), no. A3, pp. 3773–3782.
[45] P. Pritchett, "Geospace environment modeling magnetic reconnection challenge: Simulations with a full particle electromagnetic code," *J. Geophys. Res.-Space*, vol. 106 (2001), no. A3, pp. 3783–3798.
[46] M. M. Kuznetsova, M. Hesse, and D. Winske, "Collisionless reconnection supported by nongyrotropic pressure effects in hybrid and particle simulations," *J. Geophys. Res.-Space*, vol. 106 (2001), no. A3, pp. 3799–3810.

https://doi.org/10.4208/cicp.OA-2017-0102 Published online by Cambridge University Press